https://doi.org/10.5194/egusphere-2026-3365
Preprint. Discussion started: 3 July 2026

Operational XCH_4 Retrievals from MethaneSAT: Demonstrating Sensor Performance for Constraining Regional Methane Emissions

Christopher Chan Miller[1,2,3], Sébastien Roche[1,2,3], Jonas S. Wilzewski[2,3,*], Xiong Liu[3], Kelly V. Chance[3], Bingkun Luo[3], Kang Sun[4], Jonathan E. Franklin[2], Joshua S. Benmergui[2], Maya Nasr[1,2], David J. Miller[2,3,4], Sean Crowell[5], Nathan Leisso[6], Eleanor Walker[2], Ritesh Gautam[1], Nicholas LoFaso[1], Sasha Ayvazov[1], David Wells[1], Carlos Cervantes[1], Christopher Hairfield[1], and Steven Wofsy[2]

[1]Environmental Defense Fund, New York, NY
[2]Harvard John A. Paulson School of Engineering and Applied Sciences, Harvard University, Cambridge, MA, USA
[3]Center for Astrophysics | Harvard & Smithsonian, Cambridge, MA, USA
[4] Department of Civil, Structural and Environmental Engineering, University at Buffalo, Buffalo, NY, USA
[5]Department of Earth and Environmental Sciences, University of Rochester, Rochester, NY, USA
[6]BAE Systems, Inc., Boulder, CO, USA
[*]now at: EUMETSAT, Eumetsat Allee 1, 64295 Darmstadt, Germany

Correspondence: Christopher Chan Miller (cmiller@g.harvard.edu)

Abstract.

MethaneSAT, launched in March 2024, was designed to quantify regional methane (CH_4) emissions, with a primary focus on the oil and gas (O&G) sector. The satellite mission bridges the gap between coarse-resolution global flux mappers and high-resolution plume imagers by combining fine spatial resolution ($\sim 110 \times 400$ m^2 pixels at nadir), high spectral resolution (~ 0.23 nm FWHM), and a ~ 220 km swath at nadir. In this study, we present the first operational retrievals of CH_4 column-averaged dry-air mole fractions (X_{CH_4}) using the CO_2-proxy method. We assess the instrument and retrieval algorithm performance relative to the mission's precision and accuracy requirements needed to constrain CH_4 emissions at the scale of individual O&G basins.

We focus on evaluating the retrieval against four major potential sources of systematic error: albedo dependent CH_4/CO_2 column retrieval sensitivity differences, cross-track stripe biases, aerosol-induced light path errors, and subscene CO_2 variability. Tuning the a priori covariance matrix suppresses albedo-dependent errors caused by the influence of priors to sub ppb levels. Through a careful selection of homogeneous validation targets, we show that X_{CH_4} cross-track biases strongly correlate with changes in the apparent instrument spectral response function (ISRF). We develop a stripe-correction algorithm using retrieved ISRF variations in a regression model combined with wavelet-Fourier filtering to reduce stripe noise from approximately 15 ppb standard deviation to near the random noise limit.

Analysis of the homogeneous validation scenes shows that single-pixel precision is approximately 30 ppb for conditions from a typical bare-ground O&G scene (0.4 albedo, 30° SZA), corresponding to ~3 ppb at 2×2 km^2, and thus well within the mission requirement of 3 ppb at 5×5 km^2. This requirement is also met for all targeted viewing geometry/albedo combinations. Comparisons with X_{CH_4} from TROPOMI show excellent agreement, with a mean bias of 0.1 ppb and a regression slope of 0.99

https://doi.org/10.5194/egusphere-2026-3365
Preprint. Discussion started: 3 July 2026

when using X_{CO_2} from the CAMS greenhouse gas forecast as the prior in place of the GINPUT prior used operationally. The spatial pattern of Permian basin X_{CH_4} enhancements between the two instruments is highly consistent.

Observations of a Pseudo-Invariant Calibration site in Libya confirm that the CO_2-proxy approach effectively mitigates biases induced by cloud and aerosol scattering, with subscene X_{CO_2} variability emerging as the most challenging remaining error source; gradients of a few ppm can lead to X_{CH_4} errors comparable to typical basin enhancements, though such conditions appear infrequent in both MethaneSAT observations and CAMS GHG forecast simulations. Overall, MethaneSAT retrieves X_{CH_4} with the precision and accuracy required for basin-scale emissions inversion. These results suggest that the CO_2-proxy approach remains the most viable retrieval approach for regional CH_4 emission mapping, with improved treatment of subscene X_{CO_2} variability representing the key priority for future work.

1 Introduction

Reducing anthropogenic methane (CH_4) emissions is among the most effective strategies for mitigating near-term global warming, owing to its high radiative forcing and relatively short atmospheric lifetime (∼10 years) (Shindell et al., 2021). To address this urgent challenge, MethaneSAT was launched on 4 March 2024 with the goal of providing space-based constraints on regional anthropogenic CH_4 emissions, initially focusing on the oil and gas (O&G) sector.

Basin scale CH_4 emission totals are an important constraint for evaluating the effectiveness of mitigation strategies in the O&G sector. They provide an overall measure of operator performance, and can be used to track trends, compare basin-to-basin emissions, and assess progress towards commitments such as the Global Methane Pledge (United Nations Environment Programme, 2025). Mapping the spatial distribution of emissions within basins at high resolution further enables attribution to local administrative jurisdictions such as individual states, counties, and O&G sub-basins. Satellite observations are well suited for regular monitoring of basin-scale emissions due to their global coverage and revisit frequencies on daily to weekly timescales (Williams et al., 2026). However, the observing strategies of existing spaceborne instruments have not been optimized to directly quantify total emissions at the basin level and resolve their spatial distribution at the scale needed for policy-relevant regional attribution.

The number of methane plume-imaging satellites such as GHGSat (Jervis et al., 2021) and CarbonMapper (Duren et al., 2025) has expanded rapidly in recent years. These sensors provide high-spatially resolved measurements of individual CH_4 plumes, enabling attribution of large point-source emissions and supporting targeted facility-scale mitigation efforts. However, plume imagers are not designed to quantify total basin emissions, as they miss numerous smaller point sources below their detection limits, typically around 100 kg h^{-1} (Duren et al., 2025). Since smaller emission sources dispersed across wide areas can make up a significant fraction of total regional emissions (Omara et al., 2022; Williams et al., 2025), high-emitting methane plume imaging satellites with a limited field of view cannot provide a complete measure of natural gas production efficiency for the area in question. Consistent with this limitation, Cusworth et al. (2022) estimated that AVIRIS-NG, an airborne plume-imager with detection limits an order of magnitude lower than those of current satellites, captured about 35% of total CH_4

https://doi.org/10.5194/egusphere-2026-3365
Preprint. Discussion started: 3 July 2026

emissions during a comprehensive survey of US O&G basins, implying the majority of emissions were not accounted for during the measurements.

Global flux mapping satellites such as the SCanning Imaging Absorption spectroMeter for Atmospheric CartograpHY (SCIAMACHY) (Frankenberg et al., 2011), the Greenhouse gases Observing SATellite (GOSAT) series (Kuze et al., 2009; Suto et al., 2021; Tanimoto et al., 2025), and the TROPOspheric Monitoring Instrument (TROPOMI) (Hu et al., 2018) provide more accurate CH_4 observations compared to plume-imagers due to their higher spectral resolution. They have been transformative for constraining CH_4 emissions budgets at continental and global scales (Saunois et al., 2025). Their relatively coarse spatial resolution, however, limits their ability to resolve the small column-averaged enhancements characteristic of most individual production basins. Except for regions with exceptionally high emissions, such as the Permian Basin (Zhang et al., 2020; Veefkind et al., 2023; Varon et al., 2023), basin-scale signals are diluted within large satellite footprints, making it a challenge to infer basin-specific emissions totals and intra-basin emissions variability on a global scale.

MethaneSAT was designed explicitly to fill this critical observational gap by enabling direct quantification of total methane emissions across entire production basins. The instrument combines fine-spatial resolution ($\sim 110 \times 400$ m^2 pixels at nadir) with a spectral resolution (0.24 nm FWHM) comparable to that of global flux-mapping instruments such as TROPOMI (Hu et al., 2016) and GOSAT-GW (Tanimoto et al., 2025). MethaneSAT's swath width was tailored to the scale of a typical basin, spanning ~ 220 km at nadir, and $\sim$260 km on average when viewing geometry is taken into account. Narrower than a global flux mapper but wider than a plume imager, this intermediate swath concentrates pixels within the basin to achieve high spatial resolution while maintaining the coverage needed to constrain basin emissions. MethaneSAT's agile pointing system enabled regular basin revisits despite its narrower swath. The high spectral resolution enabled sensitivity to small (well below 10 ppb) column-averaged methane enhancements typical of O&G basins at MethaneSATs spatial scale. Together, this unique combination of high spatial resolution and accuracy enabled the quantification of both large point sources, as well as the sum contribution of smaller sources represented through a flux inversion. This in turn allowed basin-level emissions totals and high-resolution emission heatmaps to serve as the missions primary observational emissions products.

In this study, we present the first operational methane retrievals from MethaneSAT using the CO_2 proxy method to estimate column-averaged dry-air mole fractions of methane (X_{CH_4}). To our knowledge, this represents the first application of the proxy approach at such fine spatial resolution from space. The primary objective of this paper is to assess whether MethaneSAT can retrieve X_{CH_4} with sufficient accuracy to support robust basin-scale emissions estimation. Although the satellite mission's operations ended in June 2025 (noa, 2025), prematurely before it's design lifetime, this paper demonstrates the high-precision measurements the mission delivered to meet it's emission quantification goals. Because the basin-average and intra-basin enhancements of interest are small, systematic retrieval errors must be well controlled for MethaneSAT data to be useful for emission inversions. We therefore focus on four key sources of systematic error that are particularly relevant for basin-wide applications: (1) Retrieval vertical sensitivity differences in CO_2 and CH_4 columns, which can induce systematic errors that correlate with albedo; (2) instrument striping, which introduces spatially correlated biases in the scan direction of the satellite; (3) aerosol scattering effects, which perturb radiative transfer and the CH_4–CO_2 proxy relationship; and (4) sub-scene variability in CO_2, which challenges the assumption of spatially uniform CO_2 within the retrieval window. We evaluate the robustness

https://doi.org/10.5194/egusphere-2026-3365
Preprint. Discussion started: 3 July 2026

of the CO_2 proxy method relative to these effects and discuss implications for using MethaneSAT observations to quantify total basin methane emissions.

2 Mission Overview

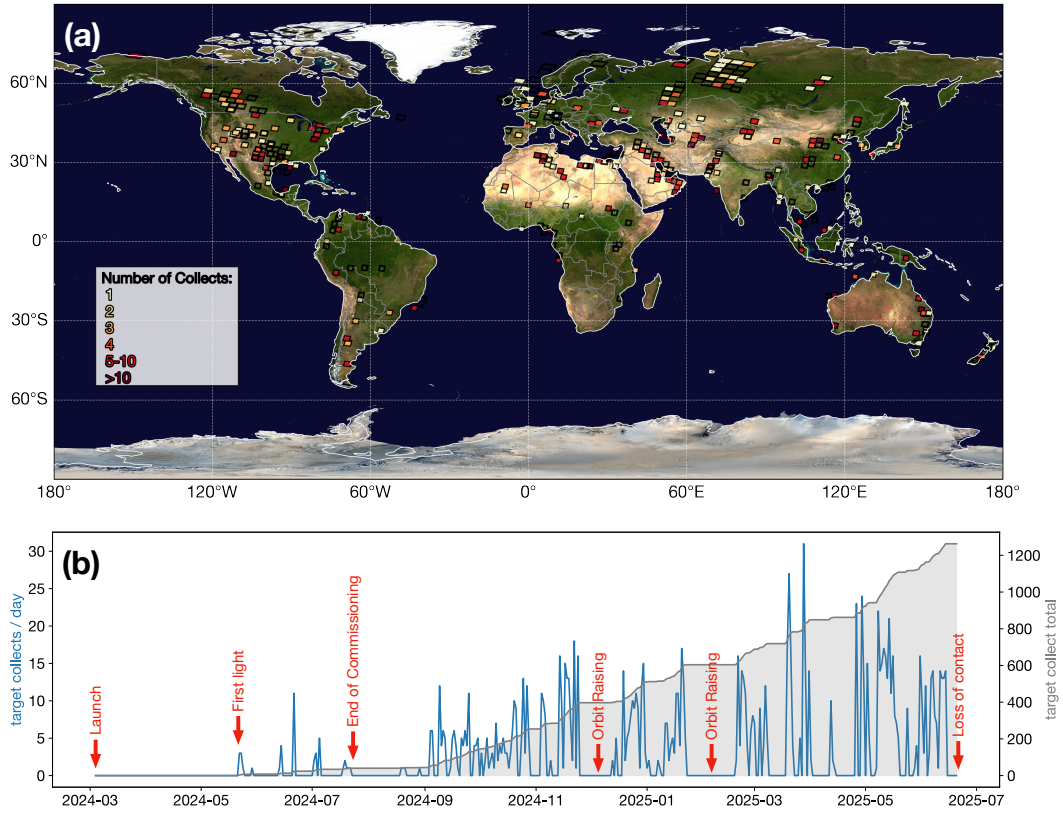

Figure 1. Overview of MethaneSAT target deck. (a) Locations as color coded by number of down-linked acquisitions over the lifetime of the mission. (b) Time series of target acquisitions with major events indicated by red arrows.

MethaneSAT consisted of a pair of Littrow-configuration grating spectrometers targeting the the $O_2(a^1\Delta_g)$ band (1249-1305 nm) and the $2\nu_3$ vibrational methane band (1598-1683 nm), with full-width at half-maximum (FWHM) spectral resolutions of 0.16 nm and 0.23 nm, respectively (Miller et al., 2026). The instrument was a pushbroom imager equipped with a custom Teledyne HgCdTe 2048×2048 pixel Focal Plane Array (FPA), of which 1,990 pixels in the spatial dimension were illuminated, providing a 21.3° field of view. The satellite was launched into a descending sun-synchronous polar orbit (equatorial crossing time: 13:45 LT) at an initial altitude of 585 km, resulting in a ground pixel size of 110×400 m^2 (across×along track) at nadir.

https://doi.org/10.5194/egusphere-2026-3365
Preprint. Discussion started: 3 July 2026

Rather than imaging continuously to achieve global coverage, MethaneSAT concentrates its detector pixels over targeted emission regions, yielding higher spatial resolution than would otherwise be achievable. This design choice necessitates a targeted acquisition strategy. Rather than continuous scanning, the satellite slewed between a set of predefined ground targets (Figure 1). Each target corresponded to a 32 s acquisition, mapping an area of approximately 220×220 km^2 at nadir. The swath width increases with viewing zenith angle (VZA), most MethaneSAT targets were observed at VZA<35° with a ~ 340 km swath width at 35°, and a few observations reached up to 55° and ~ 600 km. The primary set of targets covered regions responsible for ~90% of global oil and gas production, with additional sites selected for calibration, validation, and agricultural emissions monitoring, and some targets incidentally covering urban sources. Target scheduling was optimized using NOAA GFS forecasts (NOAA/NWS/NCEP, 2021) to reduce collecting scenes subject to high cloud cover. From first light on 22 May 2024 until the loss of communication on 20 June 2025, 1370 raw scenes were successfully downlinked, of which 1160 were processed through to level 2. Here we restrict our analysis to the 340 scenes processed with the latest algorithm version. A full reprocessing of the entire dataset is planned for later this year.

3 Retrieval Algorithm

With the exception of a stripe-correction step, the MethaneSAT retrieval algorithm is identical to that previously described for MethaneAIR (Chan Miller et al., 2024), which offers a complete description of the retrieval. Briefly, the algorithm uses the CO_2 proxy method to estimate column-averaged dry-air mole fractions of methane (X_{CH_4}). In this approach, X_{CH_4} is derived from retrieved CH_4 vertical columns (N_{CH_4}) normalized by retrieved CO_2 vertical columns (N_{CO_2}) to correct for light-path variations caused by clouds and aerosols:

$$X_{CH_4} = \frac{N_{CH_4}}{N_{CO_2}} X_{CO_2}^{model} \tag{1}$$

$X_{CO_2}^{model}$ is the a priori estimate for dry-air mole fraction of CO_2. We retrieve N_{CH_4} and N_{CO_2} from MethaneSAT radiance observations $\mathbf{y}$ using the Smithsonian Planetary Atmosphere Retrieval (SPLAT) algorithm. For MethaneSAT, SPLAT uses a non-scattering forward model $\mathbf{F}(\mathbf{x})$ within a Bayesian optimal estimation framework (Rodgers, 2000). Both N_{CH_4} and N_{CO_2} depend on the state vector $\mathbf{x}$, which includes atmospheric variables estimated from fitting $\mathbf{F}(\mathbf{x})$ to the measured spectrum $\mathbf{y}$. The configuration matches MethaneAIR (Chan Miller et al., 2024): CH_4 and CO_2 are fitted on a 19-layer vertical grid, with a scaling factor retrieved at each level, and a single scaling factor is retrieved for the water vapor profile. The state vector also includes a wavelength shift parameter, surface pressure, Chebyshev polynomial parameterizations for surface albedo and radiance offset, and two instrument spectral response function (ISRF) squeeze parameters for the CO_2 and CH_4 fit windows. For MethaneAIR the CO_2 and CH_4 fit windows were 1595-1618 nm and 1629-1654 nm respectively. For MethaneSAT this remains unchanged with the exception of the lower bound of CO_2 window because it is not covered by the satellite. Here we use the lowest valid wavelength flagged by the L1 algorithm, which is $\sim$ 1597.7-1597.8 nm depending on cross-track position.

We estimate $\mathbf{x}$ by minimizing the cost function $J(\mathbf{x})$, which balances spectral residuals against deviations from the prior $\mathbf{x_a}$:

https://doi.org/10.5194/egusphere-2026-3365
Preprint. Discussion started: 3 July 2026

$$J(\mathbf{x}) = (\mathbf{y} - \mathbf{F}(\mathbf{x}))^{\mathrm{T}} {\mathbf{S_o}}^{-1} (\mathbf{y} - \mathbf{F}(\mathbf{x})) + (\mathbf{x} - \mathbf{x_a})^{\mathrm{T}} {\mathbf{S_a}}^{-1} (\mathbf{x} - \mathbf{x_a}) \quad (2)$$

Here, $\mathbf{S_o}$ and $\mathbf{S_a}$ are the error covariance matrices for the observed spectrum and the prior state. A priori CH_4 and CO_2 profiles come from GINPUT (Laughner et al., 2023), a software first developed to generate a priori trace gas profiles for GGG2020 (Laughner et al., 2023). GINPUT is used by the Total Carbon Column Observing Network (TCCON), and the Orbiting Carbon Observatory missions, OCO-2, and OCO-3. We use meteorological inputs from GEOS-FP (Rienecker et al., 2008). Gas absorption cross sections for CH_4, CO_2, and H_2O are calculated from GGG2020 line lists (Toon, 2022a, b), which include speed-dependent Voigt profiles with line mixing for CO_2, CH_4, and O_2 (Mendonca et al., 2016, 2017, 2019).

3.1 Quality Filtering

Each retrieved pixel is accompanied by a main quality flag indicating its suitability for use. Pixels are flagged based on several criteria. Low signal is identified through the retrieval degrees of freedom for signal (DoFS), with pixels having DoFS below 0.6 for either the CO_2 or CH_4 profile state vectors excluded. Poor spectral fit quality is identified through the χ^2 statistic, using a radiance-dependent outlier threshold determined by a quantile regression applied independently at each cross-track position. This accounts for fixed calibration errors that vary across the focal plane array, and for the fact that spectral residuals are expected to scale with radiance in the presence of such errors, for example due to ISRF inaccuracies. Cloud and aerosol contamination is identified as described below.

Cloud and aerosol screening follows the approach described for MethaneAIR (Chan Miller et al., 2024), using two complementary indicators of light-path modification. The first is $O_2\Delta p$, the difference between the retrieved and a priori surface pressure, derived using a non-scattering retrieval in the $O_2(a^1\Delta_g)$ band. Absolute values of $O_2\Delta p$ greater than 20 hPa indicate pixels too impacted by aerosol/cloud scattering and are removed. This is analagous to the O_2 A-band screener used by OCO-2 (Taylor et al., 2016). The second is $\Delta X_{\mathrm{CO_2}}$, the deviation of the retrieved $X_{\mathrm{CO_2}}$ from its prior; because the CO_2 column is sufficiently well-known a priori, this provides an independent constraint for identifying light-path modifications. As an additional precaution, the $\Delta X_{\mathrm{CO_2}}$ field is bias-corrected prior to thresholding using pixels already cleared by the $O_2\Delta p$ screening, guarding against residual systematic errors in the CO_2 prior causing spurious flagging; full details of this correction will be described in a forthcoming publication. The $\Delta X_{\mathrm{CO_2}}$ indicator also provides coverage where $O_2\Delta p$ is unavailable, including a dead detector track position and pixels near the granule boundaries where the O_2 and CO_2 band footprints do not fully overlap. Prior to thresholding, total variation denoising is applied to both fields, exploiting the high spatial resolution of MethaneSAT to distinguish genuine cloud and aerosol signals from retrieval noise, an approach that is not generally feasible for instruments with coarser spatial resolution or sparser sampling.

3.2 A Priori Covariance Tuning

Because CO_2 and CH_4 mole fractions are retrieved on a vertical grid, the results are highly sensitive to the a priori covariance. This approach was preferred over using profile scale factors, which produce a retrieval response to boundary-layer enhance-

https://doi.org/10.5194/egusphere-2026-3365
Preprint. Discussion started: 3 July 2026

ments that exceeds unity. The behavior arises because the individual trace gas Jacobians are highly correlated between levels, but decrease in magnitude with height due to saturation effects from pressure broadening. Applying a uniform profile scaling shifts part of the boundary layer enhancement to the weaker-absorbing higher layers, requiring a larger overall scaling to fit the observed absorption.

During the first MethaneAIR campaign (Chan Miller et al., 2024), most observations were obtained under high-signal conditions. This was due to the high surface albedo from the mostly bare-ground regions observed, combined with the characteristically low solar zenith angles (SZA) from the late summer/early autumn campaign period. In contrast, MethaneSAT must operate across a much broader range of signal levels. The most challenging retrieval conditions correspond to boreal forests, where low signal arises from both the typically high SZA at these latitudes and the low albedo of their vegetated surfaces. To ensure robust performance under these conditions, we investigate scaling the covariance matrices for MethaneSAT using the factors $\gamma_{\mathrm{CH_4}}$ and $\gamma_{\mathrm{CO_2}}$.

$$\mathbf{S_a} = \begin{pmatrix} \gamma^2_{\mathrm{CH_4}}\mathbf{S}_{\mathrm{CH_4}} & \mathbf{0} & \mathbf{0} \\ \mathbf{0} & \gamma^2_{\mathrm{CO_2}}\mathbf{S}_{\mathrm{CO_2}} & \mathbf{0} \\ \mathbf{0} & \mathbf{0} & \mathbf{S}_{\mathrm{other}} \end{pmatrix} \tag{3}$$

Here, $\mathbf{S}_{\mathrm{CH_4}}$ and $\mathbf{S}_{\mathrm{CO_2}}$ denote the original CH_4 and CO_2 covariance matrices used in MethaneAIR, while $\mathbf{S}_{\mathrm{other}}$ represents the sub-matrix for the remaining state vector elements. The scaling factors $\gamma_{\mathrm{CH_4}}$ and $\gamma_{\mathrm{CO_2}}$ control the trade-off between precision and sensitivity to boundary-layer enhancements: larger values increase sensitivity to near-surface signals but also amplify per-pixel noise. Furthermore, the relative sensitivities to CO_2 and CH_4 must remain comparable; otherwise, CO_2 cannot serve as an effective light-path constraint, as the retrieved CO_2 and CH_4 columns will respond differently to the same light-path change.

To guide the selection of appropriate scaling factors for the satellite, we perform a linear sensitivity analysis across the observed range of signal conditions. This analysis spans expected viewing geometries (solar zenith angles: 30°-60°, viewing zenith angles: 0°-30°) and surface albedos (0.05-0.75), using a test profile from the MethaneSAT *a priori* code computed over the Permian Basin. Because prior tuning is primarily a function of radiance, these results should generalize to other profile conditions.

As the name suggests, the linear sensitivity analysis assumes that the Jacobian of the forward model ($\mathbf{K} = \frac{\partial \mathbf{F}}{\partial \mathbf{x}}$), evaluated at $\mathbf{x_a}$, is a reasonable approximation of that at the retrieved state $\hat{\mathbf{x}}$. This is almost always the case here, as the retrieval is fitting small changes in CO_2 and CH_4 above a large background, that is known accurately a priori. To estimate the $X_{\mathrm{CH_4}}$precision ($\sigma_{\mathrm{CH_4}}$), we first compute the measurement error of the state vector:

$$\mathbf{S}_{\mathrm{meas}} = \mathbf{G}\mathbf{S_o}\mathbf{G}^T \tag{4}$$

where $\mathbf{G}$ is the retrieval gain

https://doi.org/10.5194/egusphere-2026-3365
Preprint. Discussion started: 3 July 2026

$$\mathbf{G} = \frac{\partial \hat{\mathbf{x}}}{\partial \mathbf{y}} = \left(\mathbf{K}^T {\mathbf{S_o}}^{-1} \mathbf{K} + {\mathbf{S_a}}^{-1}\right)^{-1} \mathbf{K}^T {\mathbf{S_o}}^{-1} \tag{5}$$

To propagate this measurement error into a proxy precision for $X_{\mathrm{CH_4}}$, we compute the Jacobian of $X_{\mathrm{CH_4}}$ with respect to the state vector ($\mathbf{h}$):

$$\mathbf{h} = \frac{\partial}{\partial \mathbf{x}} \left(\frac{N_{\mathrm{CH_4}}(\mathbf{x})}{N_{\mathrm{CO_2}}(\mathbf{x})} X_{\mathrm{CO_2}}^{\mathrm{model}} \right) \tag{6}$$

$$= \frac{X_{\mathrm{CO_2}}^{\mathrm{model}}}{N_{\mathrm{CO_2}}} \left(\frac{\partial N_{\mathrm{CH_4}}}{\partial \mathbf{x}} - \frac{N_{\mathrm{CH_4}}}{N_{\mathrm{CO_2}}} \frac{\partial N_{\mathrm{CO_2}}}{\partial \mathbf{x}} \right) \tag{7}$$

The variance of $X_{\mathrm{CH_4}}$ is thus found through the linearized propagation of the state vector measurement uncertainty:

$$\sigma^2_{X_{\mathrm{CH_4}}} = \mathbf{h} \mathbf{S}_{\mathrm{meas}} \mathbf{h}^{\mathbf{T}} \tag{8}$$

Finally, retrieval sensitivity to boundary-layer enhancements is assessed using averaging kernels. Specifically, we use column averaging kernels, defined in SPLAT for species g as the sensitivity of the retrieved total column ($\hat{N}_{\mathrm{g}}$) to the vector of partial vertical columns ($\mathbf{n}_{\mathrm{g}}$) for each profile layer:

$$\mathbf{a}_{\mathrm{g}} = \frac{\partial \hat{N}_{\mathrm{g}}}{\partial \mathbf{n}_{\mathrm{g}}} \tag{9}$$

Figure 2 panels (a) and (b) show the CO_2 and CH_4 averaging kernels, averaged over the planetary boundary layer (PBL) and plotted as a function of radiance. The PBL is defined here as the lowest four model layers, corresponding to approximately the lowest 230 hPa. For convenience, radiance is expressed in terms of the product $A\cos(\mathrm{SZA})$, where A is the Lambertian-equivalent albedo. This quantity represents the albedo at SZA=0° that reproduces the radiance at the actual SZA. Because the averaging kernels and precision depend strongly on radiance, $A\cos(\mathrm{SZA})$ provides a convenient radiance-equivalent parameter for comparing cases across different combinations of surface albedo and viewing geometry. Each point corresponds to a retrieval simulation for a typical Permian Basin atmospheric profile, with SZA, VZA, and albedo sampled on a regular grid spanning 30-65°, 0-30°, and 0.05-0.75, respectively. The colors in Figure 2 distinguish different values of γ. In this analysis, $\gamma_{\mathrm{CO_2}}$ and $\gamma_{\mathrm{CH_4}}$ are tuned independently by fixing the other species' γ at 1. Independent tuning is possible due there being minimal spectral overlap between CO_2 and CH_4 absorption lines, which ensures that the averaging kernels of one species are largely unaffected by adjustments to the γ value of the other. Although PBL averaging kernel values are strongly dependent on radiance, they show some scatter around the main trend. This reflects residual sensitivity to SZA, as the reduction in signal at high SZA is partially offset by increased molecular absorption along the longer atmospheric path length.

To enable monitoring of high-latitude scenes, MethaneSAT must deliver reliable data for SZA values up to 65°. For a Lambertian surface, this geometry corresponds to a 60% reduction in radiance compared to nadir. Figure 2(a,b) shows that

https://doi.org/10.5194/egusphere-2026-3365
Preprint. Discussion started: 3 July 2026

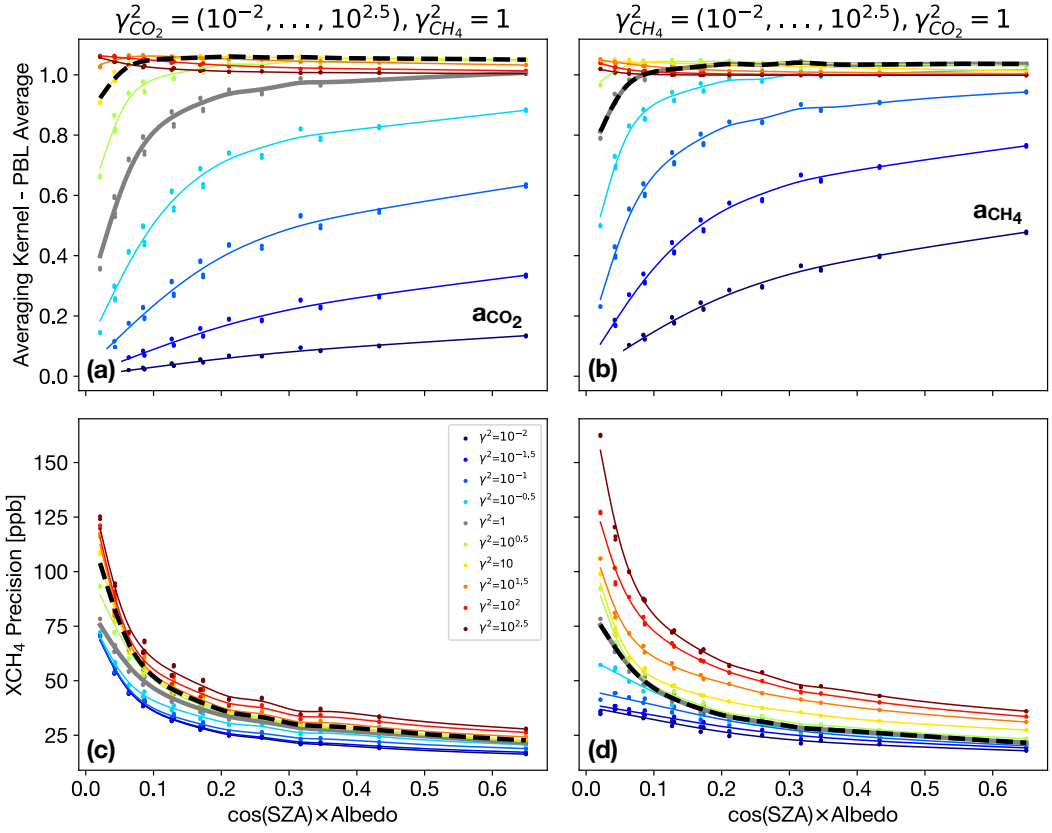

Figure 2. Sensitivity of averaging kernels (a,b) and $X_{\mathrm{CH_4}}$precision (c,d) to scaling of CO_2 (a,c) and CH_4 (b,d) prior covariance matrices. Values are computed from a linear sensitivity analysis using the MethaneSAT L1 noise model over the range of conditions observed by the satellite (colored points), with smoothing splines fitted using generalized cross-validation are shown to guide the eye. The selected tuning ($\gamma_{\mathrm{CO_2}} = 10$, $\gamma_{\mathrm{CH_4}} = 1$) indicated by the black dashed lines is chosen to produce near unity PBL averaging kernel responses over the range of expected radiance levels, here displayed in terms of solar zenith angle and Lambertian-equivalent albedo.

the original covariance matrices, $\mathbf{S}_{\mathrm{CH_4}}$ and $\mathbf{S}_{\mathrm{CO_2}}$ (grey curves), perform well for radiances typical bare-ground scenes (e.g. Permian) at moderate solar geometry ($A \approx 0.4$, SZA$\approx 30° \Rightarrow A\cos(\mathrm{SZA}) \approx 0.35$), with CO_2 and CH_4 PBL averaging kernel values close to one.

As radiance decreases, the CO_2 averaging kernel value drops faster than that of CH_4. At $A\cos(\mathrm{SZA}) = 0.063$, corresponding to the lowest-signal scene targeted by MethaneSAT (vegetated surface with $A \approx 0.15$ at SZA=65°), the CO_2 PBL averaging kernel drops to 0.72. Scaling $\mathbf{S}_{\mathrm{CO_2}}$ by $\gamma_{\mathrm{CO_2}} = 10$ brings the CO_2 averaging kernel closer to that of CH_4; an example comparing the CH_4 and CO_2 column averaging kernels before and after this scaling is shown in Figure S1.

As shown in Figure 2(c), this adjustment results in only a modest degradation of $X_{\mathrm{CH_4}}$precision for the typical bare-ground conditions ($A\cos(\mathrm{SZA}) \approx 0.35$), increasing by 4.9 ppb. For the lowest-signal case the $X_{\mathrm{CH_4}}$precision rises by 9.3 ppb; how-

https://doi.org/10.5194/egusphere-2026-3365
Preprint. Discussion started: 3 July 2026

ever, without relaxing the CO_2 constraint the retrievals will be overly influenced by the prior, leading to potential surface-dependent biases over scenes with mixed surface types.

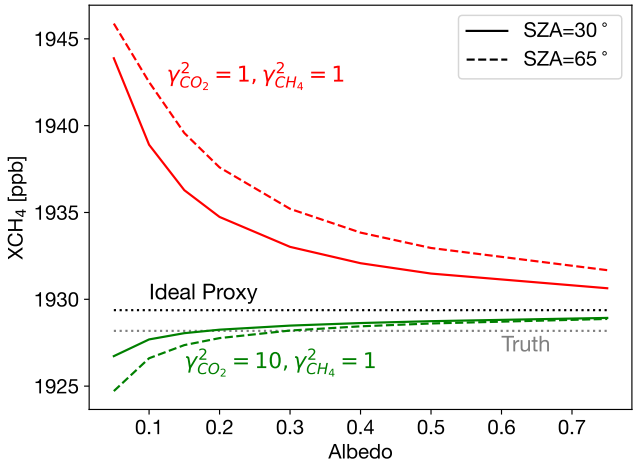

Figure 3. Theoretical albedo-dependent bias caused by influence of a priori CO_2 constraint before (red curves) and after (green curves) CO_2 a priori covariance matrix scaling for a PBL light path enhancement yielding a 2% change in vertical column. The true and ideal proxy (unity averaging kernel) $X_{\mathrm{CH_4}}$ values are also indicated. The albedo-dependence caused by the prior is substantially reduced after tuning.

To assess whether the chosen γ parameters are sufficient, we consider the impact of an aerosol within the PBL that induces a light-path enhancement. The maximum aerosol-induced perturbation to the CO_2 column after quality filtering is approximately 2%. This limit arises from the quality filtering step, which screens for cloud/aerosol scattering using retrieved surface pressure changes from the O_2 band. Observations are rejected if the retrieved pressure deviates by the prior by more than 20 hPa, corresponding to approximately 2% change in the apparent O_2 vertical column at sea level.

To simulate the light path effect, we multiply the CO_2 and CH_4 mole fractions in each PBL layer by a common scale factor f, chosen such that the total CO_2 column increases by 2%. The resulting layer enhancements are:

$$\Delta n_{\mathrm{CO_2},l} = (f-1)\, n_{\mathrm{CO_2},l} \tag{10}$$

$$\Delta n_{\mathrm{CH_4},l} = (f-1)\, n_{\mathrm{CH_4},l} \tag{11}$$

for $l \leq l_{\mathrm{PBL}}$, and zero above the PBL, where $n_{\mathrm{CO_2},l}$ and $n_{\mathrm{CH_4},l}$ are the true partial layer columns.

To emulate what MethaneSAT would retrieve ($\hat{X_{\mathrm{CH_4}}}$), we apply the averaging kernels to the change in partial layer column enhancements in CO_2 and CH_4 caused by the light path extension ($\Delta n_{\mathrm{CO_2,l}}$ and $\Delta n_{\mathrm{CH_4,l}}$ respectively):

https://doi.org/10.5194/egusphere-2026-3365
Preprint. Discussion started: 3 July 2026

$$\hat{X_{\mathrm{CH_4}}} = \frac{N_{CH_4,0} + \sum_{l=1}^{l_{\mathrm{PBL}}} a_{\mathrm{CH_4,l}} \Delta n_{\mathrm{CH_4,l}}}{N_{CO_2,0} + \sum_{l=1}^{l_{\mathrm{PBL}}} a_{\mathrm{CO_2,l}} \Delta n_{\mathrm{CO_2,l}}} X_{\mathrm{CO_2}}^{\mathrm{model}} \tag{12}$$

where $N_{CH_4,0}$ and $N_{CO_2,0}$ are the true vertical columns.

Figure 3 compares $\hat{X_{\mathrm{CH_4}}}$ retrieved using the original (red curves) and inflated $\gamma^2_{\mathrm{CO_2}} = 10$ (green curves) for a moderate (30°) and high (65°) SZA. The true $X_{\mathrm{CH_4}}$ (black line), and the idealized proxy retrieval assuming perfect averaging kernels ($\mathbf{a}_{\mathrm{CO_2}} = \mathbf{a}_{\mathrm{CH_4}} = \mathbf{1}$, grey line) are also shown. The idealized proxy differs slightly from the true $X_{\mathrm{CH_4}}$ because the light path enhancement is confined to the PBL by construction. Unlike CO_2, CH_4 mixing ratios decrease with altitude above the tropopause, so a PBL-only path length increase disproportionately enhances the apparent CH_4 column relative to CO_2, producing a small positive bias. Using the original $\mathbf{S}_{\mathrm{CO_2}}$ introduces a substantial $X_{\mathrm{CH_4}}$ smoothing error that correlates with surface albedo: the retrieved $X_{\mathrm{CH_4}}$ varies by 5.5 ppb between albedos of 0.7 and 0.15 at 30° SZA, and by 7.6 ppb at 65° SZA. After scaling $\mathbf{S}_{\mathrm{CO_2}}$ by a factor of 10, these variations are reduced to 0.8 ppb and 1.5 ppb, respectively, sufficiently suppressing prior-driven systematic errors to levels acceptable for use in the emissions inversion.

3.3 Homogeneous Validation Scene Subset

The objective of this section is to identify MethaneSAT scenes that can be treated as spatially uniform in terms of $X_{\mathrm{CH_4}}$, such that the true $X_{\mathrm{CH_4}}$ is assumed constant across the scene. These "flat-field" scenes are essential for characterizing and correcting systematic retrieval biases. The MethaneSAT target deck includes a limited number of calibration targets, which contain all but one of the Pseudo-Invariant Calibration Sites (PICS) recommended by the Committee on Earth Observation Satellites (CEOS) (Chander et al., 2013), with the excluded site removed due to its proximity to O&G emissions. The remaining PICS sites are primarily located in the Sahara desert, where CH_4 emissions are low and the sandy surface results in both uniformly high albedo across the scene and frequent elevated aerosol loadings from dust. Since retrieval biases such as cross-track striping can vary with signal strength, surface reflectance, and sun-satellite viewing geometry, relying solely on the predefined calibration targets may therefore underrepresent the range of observational conditions typically encountered. Furthermore, scenes with significant aerosol contamination must be excluded from the training dataset, as aerosol-induced cross-track variations are unrelated to the calibration errors we seek to characterize.

To improve bias characterization and correction, we expand the calibration dataset by identifying additional scenes that exhibit minimal spatial variability in $X_{\mathrm{CH_4}}$ across a broader range of observational conditions sampled by the satellite. This approach ensures that the bias-correction algorithm is trained on a more representative range of surface types and geometries.

As a first pass, we retain those scenes where at least 90% of pixels pass the main retrieval quality flag, thereby excluding cases with extensive cloud cover or poor signal. This filtering yields 81 candidate scenes.

https://doi.org/10.5194/egusphere-2026-3365
Preprint. Discussion started: 3 July 2026

Among these remaining 81 scenes, we first assess $X_{\mathrm{CH_4}}$ variability in the along-track direction to avoid noise associated with cross-track striping. For each cross-track position, we estimate the retrieval precision using the standard deviation (std) of adjacent pixel differences along-track:

$$\sigma^{\Delta_t}_{X_{\mathrm{CH_4}}}(x) = \frac{1}{\sqrt{2}}\mathrm{std}\left\{X_{\mathrm{CH_4}}[x,t] - X_{\mathrm{CH_4}}[x,t-1],:\ t \in 2,...t_{\max}\right\} \tag{13}$$

Where x and t denote the across- and along-track indices within a single MethaneSAT target collection. This metric provides a robust estimate of retrieval precision because natural $X_{\mathrm{CH_4}}$ variability occurs over spatial scales larger than a few pixels.

The natural along-track variability ($\sigma^{\mathrm{nat}}_{X_{\mathrm{CH_4}}}(x)$) is then estimated by subtracting this precision term from the along-track standard deviation of the pixel values ($\sigma^{\mathrm{pix}}_{X_{\mathrm{CH_4}}}(x)$):

$$\sigma^{\mathrm{nat}}_{X_{\mathrm{CH_4}}}(x) = \sigma^{\mathrm{pix}}_{X_{\mathrm{CH_4}}}(x) - \sigma^{\Delta_t}_{X_{\mathrm{CH_4}}}(x) = \mathrm{std}\left\{X_{\mathrm{CH_4}}[x,t]:\ t \in 1,...t_{\max}\right\} - \sigma^{\Delta_t}_{X_{\mathrm{CH_4}}}(x) \tag{14}$$

Figure 4 illustrates the along-track variability metrics for a MethaneSAT collection over the Permian Basin (Collection ID:01DF0390, September 30, 2024). The precision metric $\sigma^{\Delta_t}_{X_{\mathrm{CH_4}}}(x)$ changes by approximately 5 ppb across the scene. The worsened precision at high cross-track indices is attributable to lower surface albedo and increased detector noise beyond index 1750.

Notably, the along-track variability generated by the true $X_{\mathrm{CH_4}}$ enhancements, quantified by ($\sigma^{\mathrm{nat}}_{X_{\mathrm{CH_4}}}(x)$), is comparable in magnitude to the cross-track variation in retrieval precision near the center of the scene. This highlights the importance of accounting for the along-track variation in retrieval precision when assessing natural variability. In addition, the $\sigma^{\mathrm{nat}}_{X_{\mathrm{CH_4}}}(x)$ metric successfully captures the large plume visible in the lower left portion of the scene.

Figure 5(a) presents the sorted 97.5$^{\mathrm{th}}$ percentile values of $\sigma^{\mathrm{nat}}_{X_{\mathrm{CH_4}}}(x)$ for the 81 homogeneous validation candidate scenes. This percentile threshold was selected to ensure detection of $X_{\mathrm{CH_4}}$ enhancements spanning more than 50 cross-track positions (∼5 km). Using the elbow of the curve, we exclude scenes exhibiting elevated along-track variability. This results in removing 13 scenes with $\sigma^{\mathrm{nat}}_{X_{\mathrm{CH_4}}}(x) > 4$ ppb.

Despite this screening, some remaining scenes exhibit substantial cross-track $X_{\mathrm{CH_4}}$ gradients. To quantify these gradients, we fit a polynomial to the median along-track $X_{\mathrm{CH_4}}$ values, denoted as $X^{\mathrm{med}}_{\mathrm{CH_4}}(x)$:

$$\begin{aligned} X^{\mathrm{med}}_{\mathrm{CH_4}}(x) &= c_b\tilde{b}(x) + X_{\mathrm{bgrd}}(x) \\ &= c_b\tilde{b}(x) + \sum_{j=0}^{5} c_j T_j\left(2\frac{x - x_{\min}}{x_{\max} - x_{\min}} - 1\right) \end{aligned} \tag{15}$$

where the across-track background $X_{\mathrm{bgrd}}(x)$ is represented using a Chebyshev polynomial expansion (T_j), with the domain scaled to the valid cross-track index range ($x_{\min}$ to $x_{\max}$). The coefficients c_j capture smooth, large-scale background variability. A separate term accounts for systematic cross-track striping by scaling the median stripe pattern $\tilde{b}(x)$ with coefficient

https://doi.org/10.5194/egusphere-2026-3365
Preprint. Discussion started: 3 July 2026

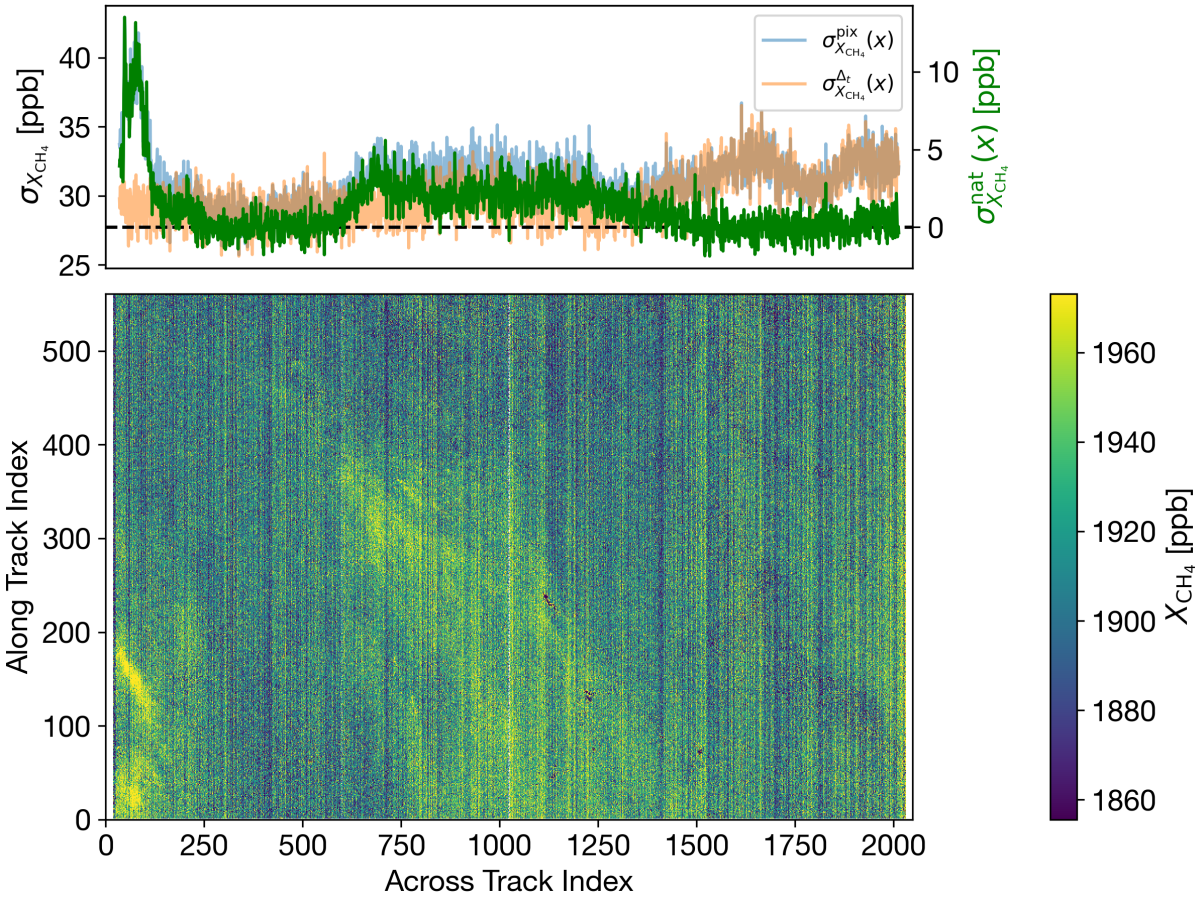

Figure 4. Demonstration of method to separate natural variability from cross-track variation in instrument precision using a scene acquired over the Permian basin (Collection ID:01DF0390, September 30, 2024). The bottom panel shows the retrieved $X_{\mathrm{CH_4}}$ before destriping. The top panel shows along-track variation computed for each cross index. The precision corresponding to each cross-track index ($\sigma^{\Delta_t}_{X_{\mathrm{CH_4}}}(x)$, orange curve) is estimated using discrete forward differences in the along-track dimension (Equation 13). Subtracting this from the along track standard deviation ($\sigma^{\mathrm{pix}}_{X_{\mathrm{CH_4}}}(x)$, blue curve) yields an estimate for the natural variation ($\sigma^{\mathrm{nat}}_{X_{\mathrm{CH_4}}}(x)$, green curve). The dashed black line indicates zero natural variation for reference.

https://doi.org/10.5194/egusphere-2026-3365
Preprint. Discussion started: 3 July 2026

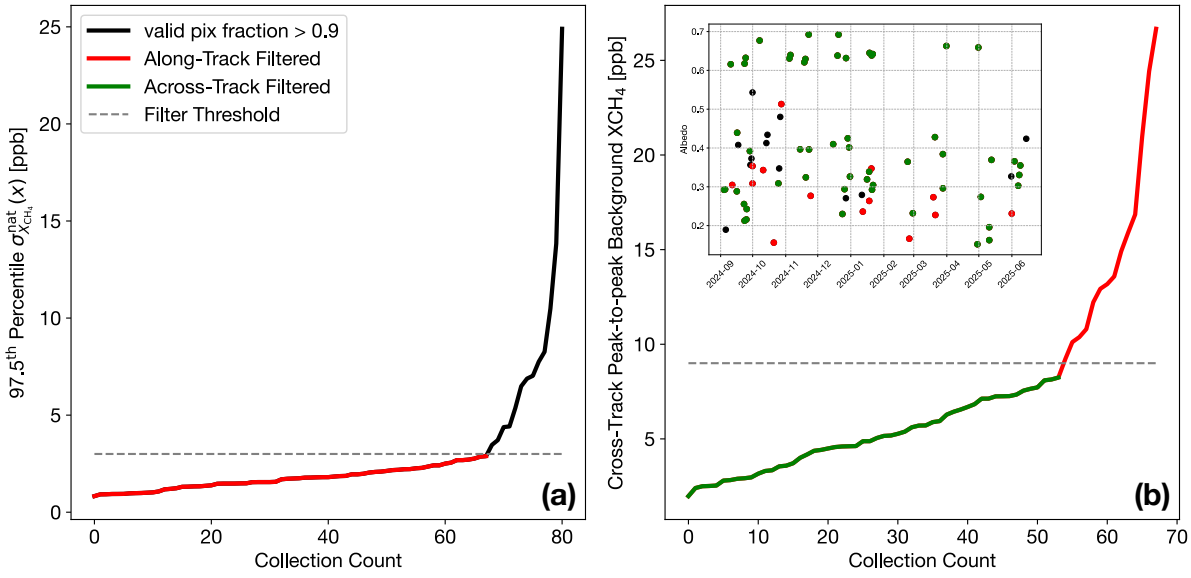

Figure 5. X_{CH_4} homogeneous validation scene selection using natural variability metrics from the 81 fully-clear candidate scenes. Panel (a) sorts scenes based on the 97.5th percentile natural variability estimated from Equation 14. Scenes with excess along-track variability are removed based on the elbow point of the curve (dashed line). Panel (b) shows the peak-to-peak difference of a polynomial fit to the along-track median of the remaining scenes (red line), used to detect excessive along-track variability. Scenes above the the elbow are removed yielding the final subset (green line). The inset panel shows the acquisition time and average albedo of scenes at each filtering stage, with black, green, and red dots indicating scenes retained after filtering for valid pixels, along-track variability, and across-track variability, respectively.

c_b. Here $\tilde{b}(x)$ denotes the median cross-track bias profile (where $\tilde{\cdot}$ denotes the median), estimated from the scenes that pass the along-track variability screening:

$$\tilde{b}(x) = \text{median}\left\{b_i(x) : i = 1, ..., i_{\max}\right\} \tag{16}$$

where $b_i(x)$ denotes the cross-track bias estimate for collection i, computed from the along-track median X_{CH_4} profile $X^{\text{med},i}_{CH_4}(x)$:

$$X^{\text{med},i}_{CH_4}(x) = \text{median}\left\{X^{i}_{CH_4}[x,t] : t \in 1, ..., t_{\max}\right\} \tag{17}$$

$$b_i(x) = X^{\text{med},i}_{CH_4}(x) - \text{mean}\left\{X^{\text{med},i}_{CH_4}(x) : x \in 1, ..., x_{\max}\right\} \tag{18}$$

Figure 5(b) shows the sorted peak-to-peak difference in the fitted background polynomials for the remaining 68 candidate scenes. Like in the first step, we apply an elbow based threshold, excluding background variations exceeding 9 ppb. The inset panel of Figure 5(b) illustrates the distribution of the final set of homogeneous validation scenes, demonstrating that this subset

https://doi.org/10.5194/egusphere-2026-3365
Preprint. Discussion started: 3 July 2026

spans a broad range of observation times and surface albedos, and therefore should provide a representative training set for the bias correction model described next.

3.4 Stripe Correction

Cross-track dependent biases are an inherent feature of data retrieved from push-broom sensors. These biases arise from calibration parameter errors, including inaccuracies in the instrument spectral response function (ISRF) and radiometric gain model. Because all observations at a given cross-track index share the same calibration errors, they exhibit an approximately constant offset that manifests as a stripe in the along-track direction. The MethaneSAT inversion framework uses data from a single target collection, making flux results more sensitive to stripe biases when compared to assimilating observations from multiple swaths. In multi-swath inversions, persistent biases can be partially averaged out as the same ground location is observed from different cross-track positions due to longitudinal variations in swath locations over time.

Most conventional stripe corrections from pushbroom instruments estimate relative biases between cross-track positions using along-track smoothing, with window sizes chosen to be short enough to capture variation in stripe errors while still suppressing real $X_{\mathrm{CH_4}}$variability in the smoothed values (Borsdorff et al., 2018; Hasekamp et al., 2025). These methods require continuous latitudinal coverage, where viewing geometries and signal strengths vary smoothly along the orbit. In contrast, MethaneSAT observations are collected sporadically, with large scene-to-scene changes in sun-satellite geometry and signal. Because stripe biases depend on these factors, such approaches would have to be applied independently to each scene. However this is not usually possible as the intrinsic $X_{\mathrm{CH_4}}$variability within individual scenes is too large to reliably separate stripe errors from real atmospheric signals.

Instead we build a regression model for the stripe biases using the subset of homogeneous validation scenes described in the previous section. These scenes span a wide range of viewing conditions, time periods, and radiance levels, and thus are expected to represent the conditions encountered across the full dataset.

We first estimate the across-track bias ($b(x)$) by assuming the true $X_{\mathrm{CH_4}}$ is constant across the scene, using Equation 18. Figure 6(c1) shows $b(x)$ for the homogeneous validation scenes, sorted in time and ordered by collection index. The mean 1σ variability in $b(x)$ across all the homogeneous validation scenes is 16 ppb, similar in magnitude to a typical O&G basin enhancement. Subtracting the median pattern reduces the residual variability in the homogeneous validation data by about half (7.7 ppb). While this represents a significant improvement, the remaining error is too high to meet the missions systematic error requirements.

To understand the major patterns of variability in the observed stripe bias, we performed a principal component analysis. Here the stripe bias patterns are reprojected onto an orthoganal basis of principal components $\mathbf{p}_j$, ordered by the fraction of total variance they explain. The stripe pattern $\mathbf{b}_i$ (the vector form of $b_i(x)$) from collection i can be expressed in terms of principal components as:

$$\mathbf{b}_i = \overline{\mathbf{b}} + \sum_j c_{ij}\mathbf{p}_j \tag{19}$$

https://doi.org/10.5194/egusphere-2026-3365
Preprint. Discussion started: 3 July 2026

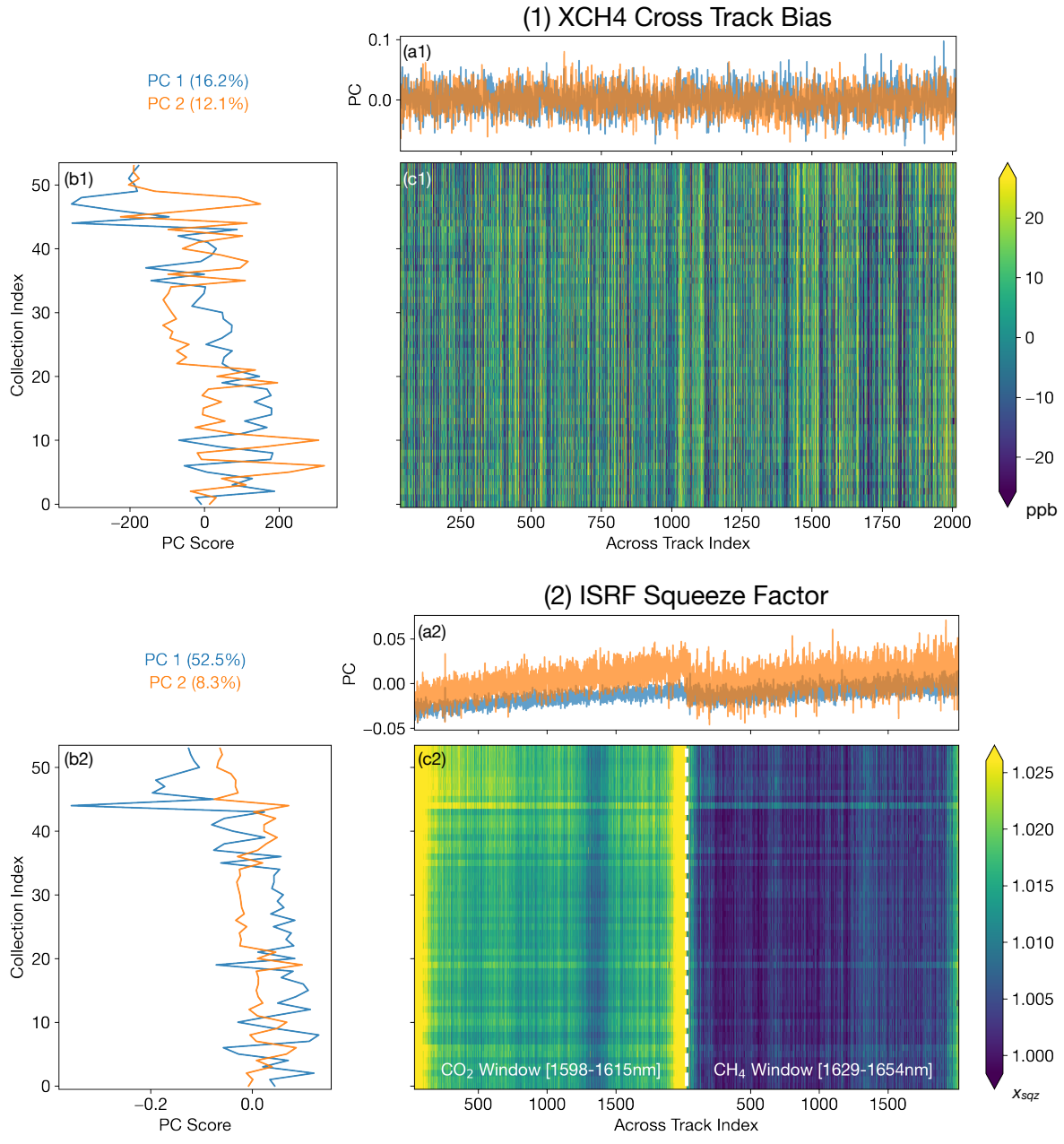

Figure 6. Analysis of (1) cross-track stripe bias ($b(x)$) and (2) ISRF variability for homogeneous validation scenes. Panels (c1,c2) show the along-track medians for all homogeneous validation scenes, sorted in time and ordered by collection index. Panels (a1) and (b1) show the first two principal components and component scores for $b(x)$. the corresponding values for the ISRF squeeze principal component analysis is shown in (a2),(b2), with the variability explained by each component indicated above.

https://doi.org/10.5194/egusphere-2026-3365
Preprint. Discussion started: 3 July 2026

where $\overline{\mathbf{b}}$ is the mean stripe pattern across all collections and c_{ij} is the score for principal component j.

Figure 6(a1) and (b1) show the first two principal components and their corresponding scores for the observed stripe bias. Together these explain 38% of the variation in the stripes. The PC scores show slow drifts in the stripe pattern over the course of the mission, overlayed with large collection-to-collection variability.

We previously performed a similar PCA analysis of MethaneAIR data (Chan Miller et al., 2024). In that case the time evolution of the stripe bias PC scores was considerably smoother. We showed that the stripe bias was primarily driven by gradual changes in instrument focus, induced by temperature variations during flight.

For MethaneAIR we accounted for this defocus by fitting ISRF squeeze factors ((x_{sqz}) to the CO_2 and CH_2 fit windows. These factors stretched or squeezed the laboratory-derived ISRF table ($\Gamma_{\mathrm{TAB}}(\lambda)$. The retrieved ISRF $\Gamma(\lambda)$ is given by:

$$\Gamma(\lambda) = \Gamma_{\mathrm{TAB}}(x_{sqz}\lambda) \tag{20}$$

Including these squeeze factors in MethaneAIR reduced but did not fully eliminate drifts in the cross-track $X_{\mathrm{CH_4}}$ bias pattern. This is expected because squeezing the ISRF table is not a perfect model for the actual optical changes. Nevertheless, because x_{sqz} tracked the defocus change, it is a good predictor for the remaining stripe bias. We incorporated it into a Partial Least Squares (PLS) regression model to successfully remove most of the remaining variability.

For MethaneSAT we retained the ISRF squeeze parameters in the retrieval to account for any on-orbit changes. The ISRF squeeze factors for the homogeneous validation scenes are shown in Figure 6(c2), along with their first two principal components and scores ((c1) and (c3) respectively). We expect much smaller defocusing impacts due to better on-orbit thermal control (Miller et al., 2026) compared with those observed for MethaneAIR. This is consistent with CH4 band ISRF width changes on-orbit of $<$2% compared with ground-based calibration observations (Miller et al., 2026), which are an order of magnitude lower than the corresponding values for MethaneAIR ($\sim$10%). Furthermore, on-orbit MethaneSAT ISRF widths were more stable ($<$0.4% changes) over time. The on-orbit change in ISRF is more pronounced in the CO_2 window, with a narrowing of up to 3% relative to ground-based, calibration-derived ISRFs at the cross-track edges of the FPA. The larger change in the CO_2 window is expected because the window abuts the edge of the FPA, making it more sensitive to shifts in focus that may have occurred during launch.

There are also two stable anomalies centered at cross-track indices 650 and 1350. During instrument line shape ground-based calibration, only a fraction of the slit was illuminated at one time and there was limited overlap between the three partial field of view illumination extents (Miller et al., 2026). Although merging algorithms reduced artifacts for overlapping spatial position illuminations, the on-orbit data suggest that small discontinuity errors remain for ISRFs at the overlap positions (Miller et al., 2026).

As with $b(x)$, the ISRF exhibits large scene-to-scene variability, which appears to be associated with radiance. Figure 7 shows the score of the leading ISRF principal component as a function of radiance, with points color-coded by observation time. This component alone explains over half the variability in ISRF over the homogeneous validation scenes. The component score decreases with increased radiance, corresponding to a broadening of the ISRF at higher signal levels. An in-band stray-

https://doi.org/10.5194/egusphere-2026-3365
Preprint. Discussion started: 3 July 2026

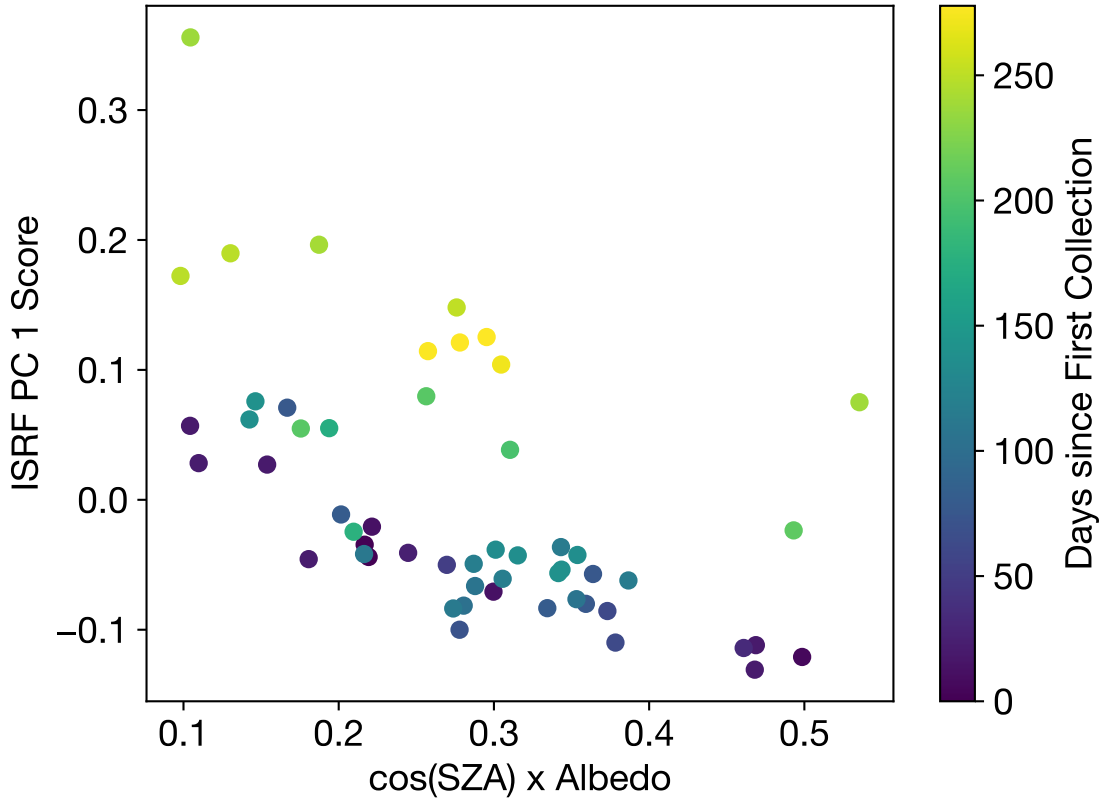

Figure 7. Relationship between ISRF variability, scene radiance, and time over the homogeneous validation dataset. The score of the leading ISRF principal component is shown as a function of scene radiance, with points colored by observation time.

light correction was implemented for the instrument line shape exposures prior to deriving the ISRF lookup table (Miller et al., 2026), though stray-light correction was not applied to level 1 radiances for the flat field scenes presented in this study. Future analysis including stray-light correction of all scenes via convolution with the ∼3% peak integrated stray-light kernel (Miller et al., 2026) will be helpful to determine whether this is the dominant cause of the variation shown here.

The scene-to-scene variability of ISRF is also strongly correlated with variability in $b(x)$. The Pearson correlation coefficients between the scores of the leading and the second principal components of the two datasets are 0.82, and 0.74 respectively, indicating that the retrieved ISRF squeeze have good predictive power for $b(x)$. We therefore employ the same PLS regression model as MethaneAIR. Here relationships between predictors and responses are determined by projecting them onto latent components that maximize covariance, effectively handling collinearity. We select the number of components (9) using k-fold cross-validation combined with permutation testing. Full methodological details are provided in Section S2 in the supplement.

https://doi.org/10.5194/egusphere-2026-3365
Preprint. Discussion started: 3 July 2026

Because the retrieved ISRF is independent of $X_{\mathrm{CH_4}}$, the PLS model trained on the homogeneous validation scenes can be used to predict $b(x)$ even for scenes with large $X_{\mathrm{CH_4}}$ variability.

To measure the effectiveness of the PLS model at reducing stripe noise, we define a scene-based stripe metric σ_b, which estimates the standard deviation of the cross-track bias $b(x)$. To minimize the influence of subscene $X_{\mathrm{CH_4}}$ variability, σ_b is derived from cross-track finite differences $\Delta^x X_{\mathrm{CH_4}}(x,t)$:

$$\Delta^x X_{\mathrm{CH_4}}(x,t) = X_{\mathrm{CH_4}}[x,t] - X_{\mathrm{CH_4}}[x-1,t] \tag{21}$$

$\Delta^x X_{\mathrm{CH_4}}(x,t)$ is influenced by both retrieval precision and cross-track bias differences between tracks x and $x-1$. To reduce the influence of random errors associated with retrieval precision, we take the median along-track:

$$\widetilde{\Delta^x X_{\mathrm{CH_4}}}(x) = \mathrm{median}\left\{\Delta^x X_{\mathrm{CH_4}}(x,t) :\ t \in 1,...,t_{\max}\right\} \tag{22}$$

The resulting quantity $\widetilde{\Delta^x X_{\mathrm{CH_4}}}(x)$ approximates the discrete derivative of $b(x)$. Accounting for the variance amplification introduced through differencing, we estimate the standard deviation of $b(x)$ as:

$$\sigma_b = \frac{1}{\sqrt{2}}\mathrm{std}\left\{\widetilde{\Delta^x X_{\mathrm{CH_4}}}(x) :\ x \in 1,...,x_{\max-1}\right\} \tag{23}$$

Figure 8 shows the histogram of σ_b from Eq. 23 for all scenes with at least 80% clear pixels ($n = 114$). Scenes with heavy cloud contamination are excluded, as cloud-induced $X_{\mathrm{CH_4}}$ variability strongly inflates σ_b. The mean σ_b for raw $X_{\mathrm{CH_4}}$ (blue histogram) is 15 ppb, consistent with 16 ppb from homogeneous validation scenes (Fig. 6), providing an independent validation for our σ_b estimation method.

The grey dashed line in Fig. 8 indicates σ_b for a scene with 35 ppb Gaussian noise, representative of typical single-pixel precision. This value (σ_b =3.5 ppb) represents the theoretical lower limit for a perfect stripe correction. Applying the PLS-based correction (orange histogram) substantially reduces stripe noise, yielding a mean σ_b of 6.1 ppb. While this represents a significant improvement, the residual noise remains above the random-noise limit. We therefore apply an additional destriping step using the wavelet-based method of Schneising et al. (2023).

An overview of the full destriping procedure is shown in Figure 9 for an example scene over the Permian. Let $X^{\mathrm{ref}}_{\mathrm{CH_4}}$ denote the $X_{\mathrm{CH_4}}$ field after subtracting the PLS-predicted stripe bias pattern predicted from the retrieved ISRF (labeled "PLS Correction" in Figure 9). We first perform a two-dimensional multilevel wavelet decomposition with symmetric boundary conditions, separating horizontal (h), vertical (v), and diagonal (d) details:

$$X^{\mathrm{ref}}_{\mathrm{CH_4}}(x,t) = \sum_{m,n} a_{L,m,n}\,\phi_{L,m,n}(x,t) + \sum_{b\in\{h,v,d\}}\sum_{l=1}^{L}\sum_{m,n} b_{l,m,n}\,\psi_{b,l,m,n}(x,t), \tag{24}$$

https://doi.org/10.5194/egusphere-2026-3365
Preprint. Discussion started: 3 July 2026

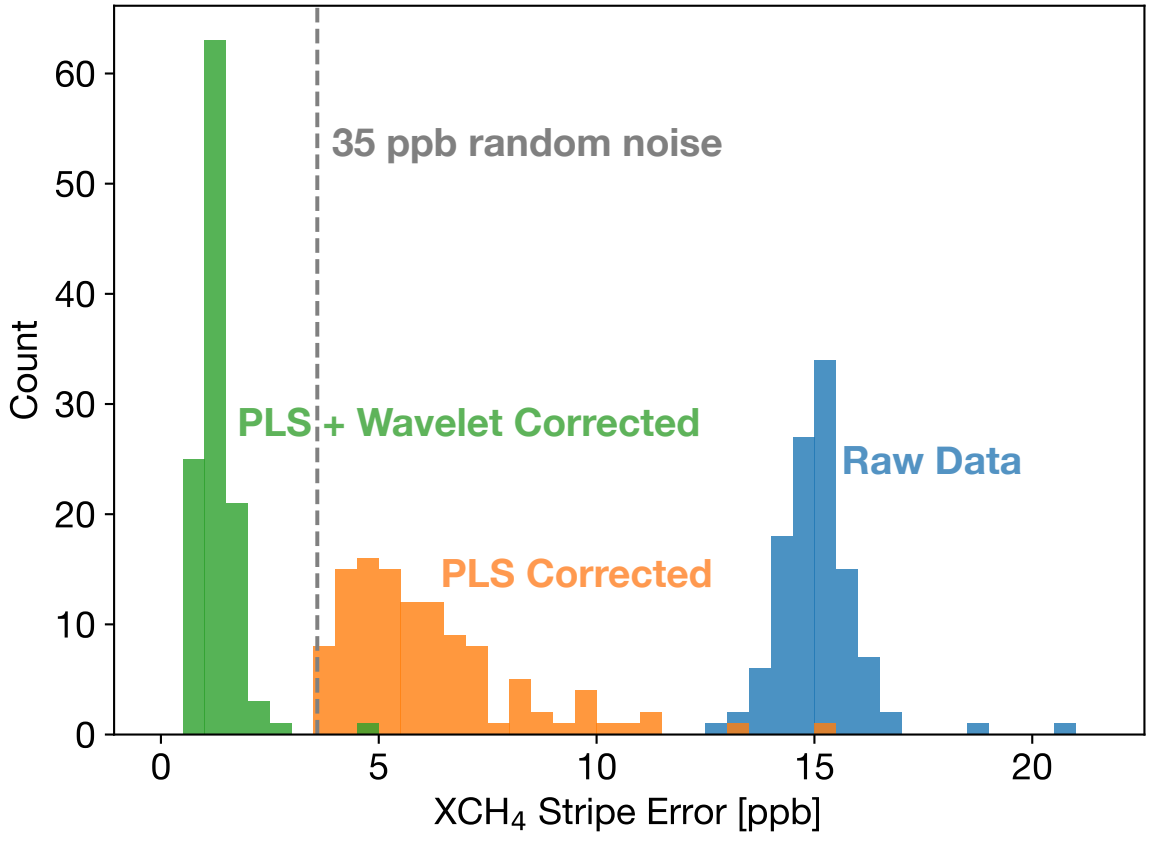

Figure 8. Histogram of $X_{\mathrm{CH_4}}$ stripe bias standard deviation for all MethaneSAT clear scenes (clear pixel fraction > 80%). The standard deviation is estimated for each scene using Equation 23. Histograms are shown for $X_{\mathrm{CH_4}}$ prior to correction (blue), after the PLS correction (orange) and after final application of the wavelet filter (green). The σ_b computed for for a scene containing only 35 ppb white noise typical of the single-pixel precision is indicated by the dashed line. The histogram of a perfect stripe correction should be centered around this line.

https://doi.org/10.5194/egusphere-2026-3365
Preprint. Discussion started: 3 July 2026

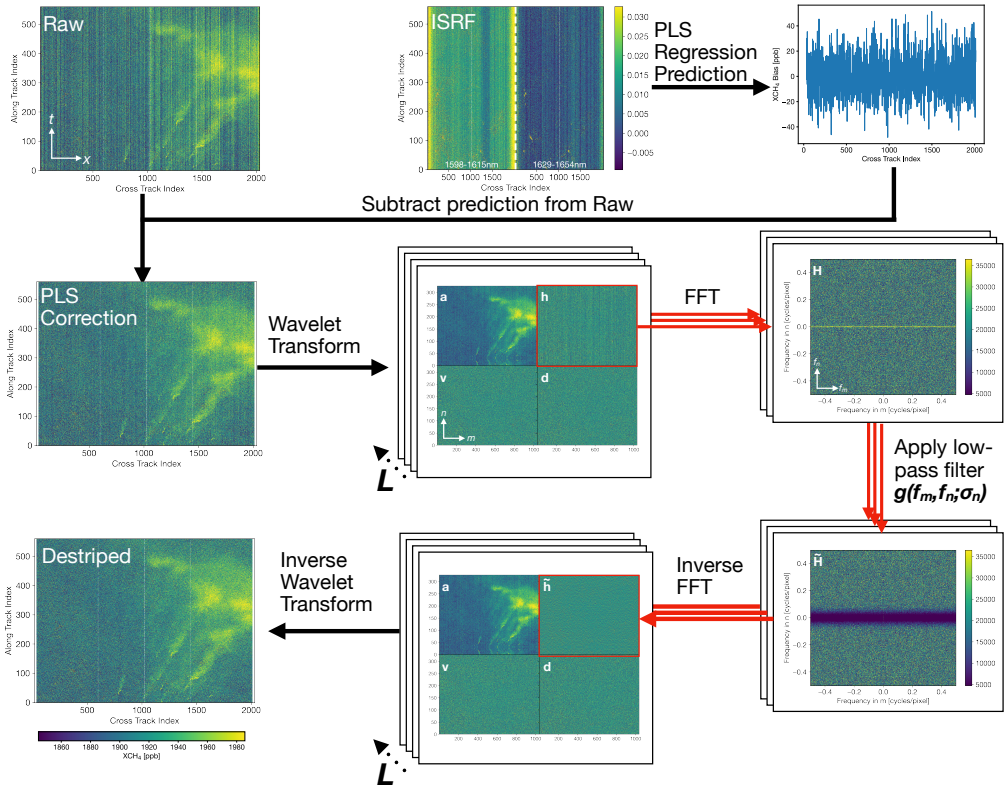

Figure 9. Schematic overview of the MethaneSAT destriping procedure for an example scene over the Permian Basin. The input X_{CH_4} field is first corrected using the partial least squares (PLS) model based on retrieved ISRF parameters, yielding the "PLS Correction" field. This is then decomposed using a multilevel 2D wavelet transform. Stripe artifacts, contained primarily in the horizontal detail components are suppressed using a frequency-domain filter before inverse wavelet reconstruction of the destriped image.

https://doi.org/10.5194/egusphere-2026-3365
Preprint. Discussion started: 3 July 2026

where $\phi_{L,m,n}(x,t)$ is the scaling function and $\psi_{b,l,m,n}(x,t)$ are the wavelet basis functions. We use 16^{th} order Coiflets following Schneising et al. (2023). The parameter L controls the the number of decomposition levels, each level a discrete wavelet decomposition of the scaling function from the previous step. L largely controls the average degree of stripe suppression. Based on tests using synthetic stripe patterns with amplitudes matching the post-PLS residuals (Section S2.1), we set $L = 7$, which reduces residual stripe noise to below 1 ppb. This choice is consistent with that of Schneising et al. (2023).

The stripes are predominantly encoded in the horizontal detail components $h_{l,m,n}$. These components are filtered using a Fourier-based low-pass filter. Let H_{l,f_m,f_n} denote the 2D Fourier transform of $h_{l,m,n}$. Stripe energy is concentrated along the cross-track direction, corresponding to $f_n = 0$, as seen in Figure 9. We define the band pass filter $g(f_m, f_n)$ as:

$$g(f_m, f_n) = \begin{cases} 1, & f_m = 0, \\ 1 - \exp\left(-\frac{f_n^2}{\sigma_{f_n}^2}\right), & f_m \neq 0, \end{cases} \tag{25}$$

where the special treatment of $f_m = 0$ ensures the mean offsets in the horizontal detail component are preserved (Münch et al., 2009). The parameter σ_{f_n} controls the range of along-track frequencies retained by the filter: it must be large enough to capture along-track variations in the stripe biases, while remaining small enough to preserve geophysical structures in the X_{CH_4} field. Based on tests using synthetic Gaussian plumes and comparisons with real scenes (Section S2.2), we set $\sigma_{f_n} = 0.05$ cycles/pixel. The filtered coefficients are then given by

$$\widetilde{H}_{l,f_m,f_n} = g(f_m, f_n) H_{l,f_m,f_n} \tag{26}$$

The filtered horizontal detail coefficients $\widetilde{h}_{l,m,n}$ are then obtained via the inverse Fourier transform of $\widetilde{H}_{l,f_m,f_n}$. The destriped X_{CH_4} field is then computed by replacing the original $h_{l,m,n}$ with $\widetilde{h}_{l,m,n}$, and then performing the inverse wavelet transform.

The resulting distribution of σ_b after PLS and wavelet-based destriping is shown by the green histogram in Figure 8. The residual stripe noise falls below the level expected from purely random, normally distributed noise. This behavior is expected, as the band-pass filter $g(f_m, f_n)$ suppresses a subset of Fourier modes. Random noise is spatially uniform in the Fourier-transformed horizontal detail component (H; Figure 9), thus yielding increased denoising with increases in σ_{f_n}.

4 Validation

In this section, we evaluate whether the MethaneSAT L2 product meets its mission performance requirements. A unique aspect of the MethaneSAT mission was the mandate that an emissions product be part of the operational processor, which established specific precision and accuracy goals for the X_{CH_4} retrieval. The pre-launch precision requirement was 3 ppb at a spatial scale of 5×5 km^2, based on emissions inversion Observing System Simulation Experiments (OSSEs) conducted during mission planning. Alongside this precision goal, MethaneSAT also has stringent accuracy requirements. As noted in the introduction, systematic biases must be controlled at the ppb level to remain well below typical basin-scale CH_4 enhancements.

https://doi.org/10.5194/egusphere-2026-3365
Preprint. Discussion started: 3 July 2026

Major potential sources of systematic error include cross-track striping, aerosol interference, and subscene CO_2 variability. In the previous section, we developed and applied a stripe-correction approach that reduces cross-track bias uncertainties to within these requirements. Here, we assess aerosol interference using homogeneous validation scenes and evaluate overall accuracy through intercomparisons with TROPOMI. Finally, we use CAMS CO_2 fields to assess whether subscene CO_2 gradients could introduce systematic uncertainties exceeding mission requirements.

4.1 MethaneSAT Precision

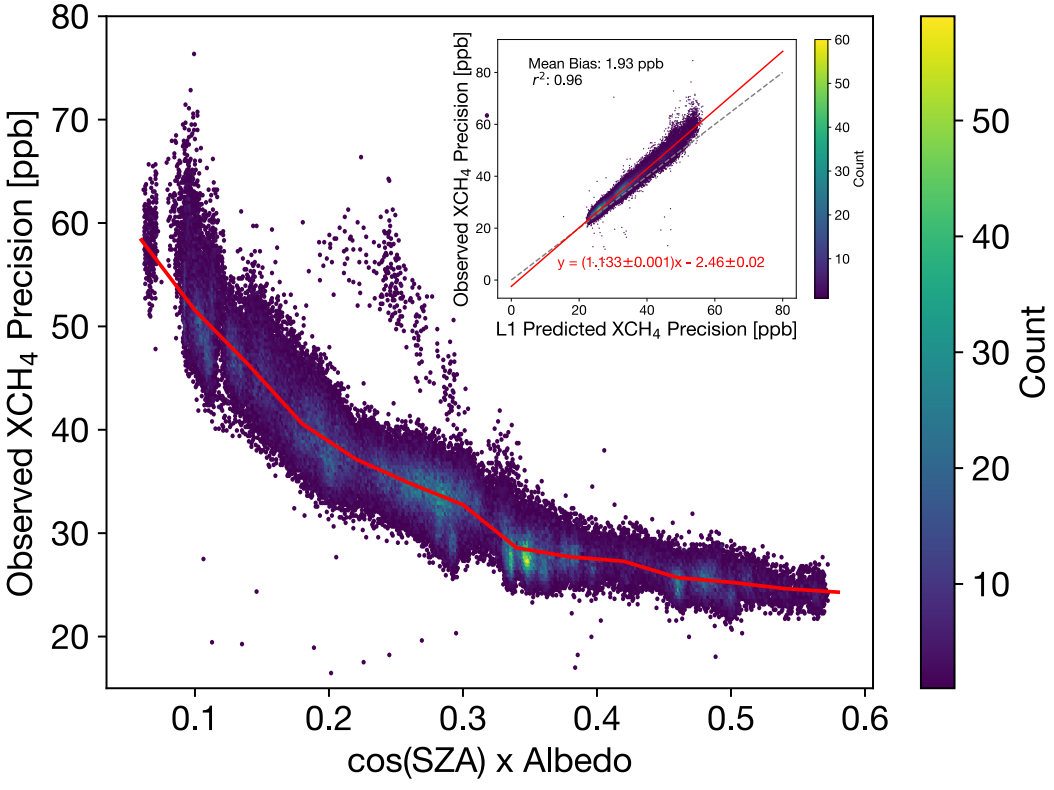

Figure 10. Observation-derived $X_{\mathrm{CH_4}}$ precision as a function of radiance (expressed as lambertian-equivalent albedo multiplied by SZA) for the homogeneous validation scenes identified in Section 3.3. Precision is computed for each cross-track index using along-track finite differences (Equation 13). The inset compares the observation-derived precision with the theoretical estimate from the measurement covariance matrix (Equation 8) for validation of the observation-derived estimate.

Here we assess MethaneSAT $X_{\mathrm{CH_4}}$ precision using the subset of homogeneous validation scenes identified in Section 3.3. Figure 10 shows the observation-derived estimate of $X_{\mathrm{CH_4}}$ precision as a function of radiance. For each scene, $X_{\mathrm{CH_4}}$ precision is computed for each cross-track index using along-track finite difference method used to identify the homogeneous validation scenes (Equation 13). The inset panel compares the observation-derived precision with the theoretical estimate

https://doi.org/10.5194/egusphere-2026-3365
Preprint. Discussion started: 3 July 2026

from the measurement covariance matrix (Equation 8). The agreement is good, with a mean bias of 1.93 ppb, indicating strong self-consistency between the Level 1 and 2 products and supporting the reliability of the observation-based precision estimates.

As expected, X_{CH_4} precision depends strongly on signal. For a representative bare-ground scene (albedo 0.4, solar zenith angle 30°), such as the Permian Basin, the single-pixel X_{CH_4}precision is approximately 30 ppb. This corresponds to a precision of better than 3 ppb when aggregated to 2×2 km^2, far exceeding the pre-launch requirement set at 5×5 km^2. For more challenging observing conditions, such as boreal forest scenes at high solar zenith angle (albedo 0.15, SZA 60°), the single-pixel precision is approximately 56 ppb, yielding a precision of 2.3 ppb at 5×5 km^2. These results demonstrate that MethaneSAT meets, and in most cases exceeds, its pre-launch precision requirements.

4.2 TROPOMI Intercomparison

We compare MethaneSAT to TROPOMI X_{CH_4} retrievals of version ≥2.7.1, (from 8 September 2024), restricting the intercomparison to this version as earlier versions did not include a stripe correction. Uncorrected Stripes in TROPOMI X_{CH_4}can reach several percent, introducing significant errors for individual colocations since a typical MethaneSAT target spans only 15–20 TROPOMI cross-track pixels. Although TROPOMI exhibits larger systematic biases than GOSAT, its daily coverage and similar equatorial crossing time to MethaneSAT (13:45LT vs 13:00LT for TROPOMI) allow colocations for most targets within a few hours. Recent TROPOMI algorithm improvements, such as an empirical albedo correction (Lorente et al., 2021) and a higher-order albedo polynomial in the spectral fit (Lorente et al., 2023) have reduced spatial biases. The mean bias relative to TCCON is most recently reported as -5.6 ppb (Lorente et al., 2023).

To compare the datasets, we aggregate MethaneSAT X_{CH_4}onto the TROPOMI L2 swath grid using point-in-polygon sampling. This introduces negligible error because MethaneSAT pixels are much smaller (∼1000 per TROPOMI pixel). The aggregated MethaneSAT precision is ∼1–2 ppb, an order of magnitude better than TROPOMI. We only include aggregated MethaneSAT pixels when the mean surface pressure is within 10 hPa of the corresponding TROPOMI pixel, MethaneSAT covers at least half the TROPOMI pixel area, and the two observations are separated by no more than 2 hours. Applying these criteria yields 85,824 matched TROPOMI–MethaneSAT pixel pairs. To minimize the influence of differing priors, we apply the MethaneSAT prior to TROPOMI (Rodgers and Connor, 2003), which has a relatively small effect (mean $\pm$ 1σ: 0.8 ± 2.0 ppb).

Figure 11 shows all valid overlapping pixels between MethaneSAT and TROPOMI in the processed dataset using the operational GGG2020 prior (panels a-b; the CAMS prior comparison is shown in the same figure and discussed below). The overall agreement is strong, with a mean bias of 0.1 ppb. The regression slope is slightly high (1.069), driven by differences in the Southern Hemisphere where MethaneSAT averages about 8 ppb lower than TROPOMI, compared to a +2 ppb bias in the Northern Hemisphere.

The small discrepancies between the datasets may be related to the difference in retrieval method. Since MethaneSAT uses the CO_2 proxy approach, the retrieved $X_{CH_4}$is dependent on the CO_2 prior used to translate the column density ratio. The difference between the true and retrieved column ($\hat{X}_{CH_4} - X_{CH_4}$) induced by the prior directly scales with the error in the CO_2 apriori mole fraction ($X_{CO_2,\text{prior}} - X_{CO_2}$):

https://doi.org/10.5194/egusphere-2026-3365
Preprint. Discussion started: 3 July 2026

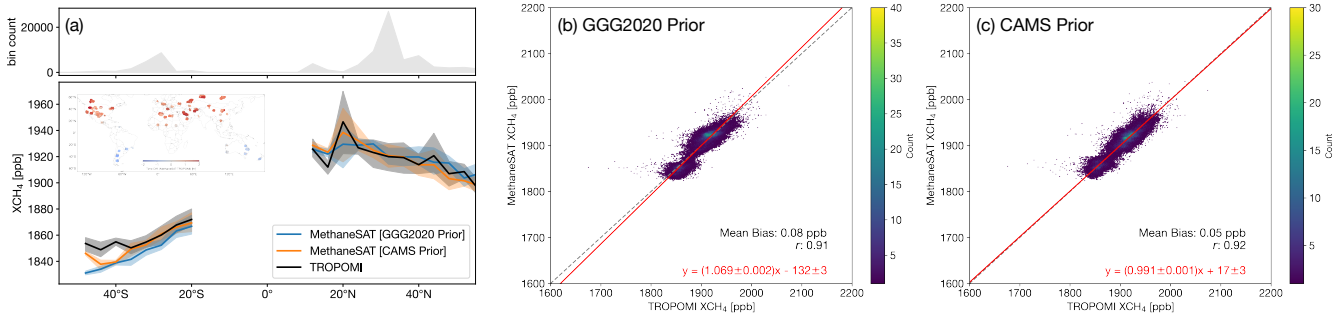

Figure 11. Comparison of overlapping X_{CH_4} retrievals from MethaneSAT and TROPOMI for all valid coincident pixels in the processed dataset. (a) MethaneSAT-TROPOMI coincidences binned in 4° latitude bands for the GGG2020 and CAMS X_{CO_2} priors. (,c) Scatterplot of the coincidences along with reduced major axis regression fit for the GGG2020 (b) and CAMS (c) priors.

$$\hat{X}_{CH_4} - X_{CH_4} = \frac{\hat{N}_{CH_4}}{\hat{N}_{CO_2}} \left(X_{CO_2,\text{prior}} - X_{CO_2}\right) \tag{27}$$

For typical X_{CO_2} and X_{CH_4} values observed today (425 ppm and 1900 ppb respectively), a 1 ppm error in X_{CO_2} translates to a ~ 4.5 ppb error in X_{CH_4}. The GGG2020 X_{CO_2} prior used by MethaneSAT is designed to predict background values. It is therefore conceivable that some of the discrepancy is driven by not accounting for the influence of local sources in the prior, as it would only require enhancements a few ppm above background to explain the differences between the datasets. In order to test the sensitivity to the prior choice, we recomputed the proxy X_{CH_4} (Equation 1) using a priori X_{CO_2} from the CAMS global greenhouse gas forecast (Copernicus Atmosphere Monitoring Service, 2024) as $X_{CO_2}^{\text{model}}$. CAMS integrates GOSAT and IASI CH_4 and CO_2 observations into the ECMWF Integrating Forecasting System (IFS) weather forecasting model, using 4 dimensional variational data assimilation. Figure 11(a) (orange line) and (c) show the same comparison after adjusting X_{CH_4} using the CAMS prior. In general the agreement is remarkably good. The negative bias in the Southern Hemisphere reduces from 8 ppb to 1.4 ppb, reducing the linear regression slope from 1.069 to 0.991.

Although the improvement in absolute column values is better for CAMS, we keep the GGG2020 prior in the operational product. Firstly, the emissions inversion algorithm will be insensitive to a uniform X_{CO_2} prior error across the scene, as it infers emissions from local X_{CH_4} enhancements which will be scaled proportional to the fractional error in X_{CO_2}. Secondly, it is unlikely that CAMS can properly capture the true subgrid X_{CO_2} variations at the scale of a MethaneSAT target, and thus may induce an additional source of systematic error in the retrieved X_{CH_4}. We will return to the issue of subscene CO_2 variability in Section 4.4. We note that when using MethaneSAT data for an application that requires good consistency in X_{CH_4} values across collections rather than individual collection enhancements, the CAMS prior is likely more reliable.

Permian Basin X_{CH_4} emissions are sufficiently large to be detected by TROPOMI in a single overpass, enabling comparison of X_{CH_4} enhancements with MethaneSAT. Figure 12 shows all MethaneSAT scenes within one hour of the nearest TROPOMI overpass and with at least 80% cloud-free coverage. Overall, both instruments identify similar emission hotspots, with Pearson

https://doi.org/10.5194/egusphere-2026-3365
Preprint. Discussion started: 3 July 2026

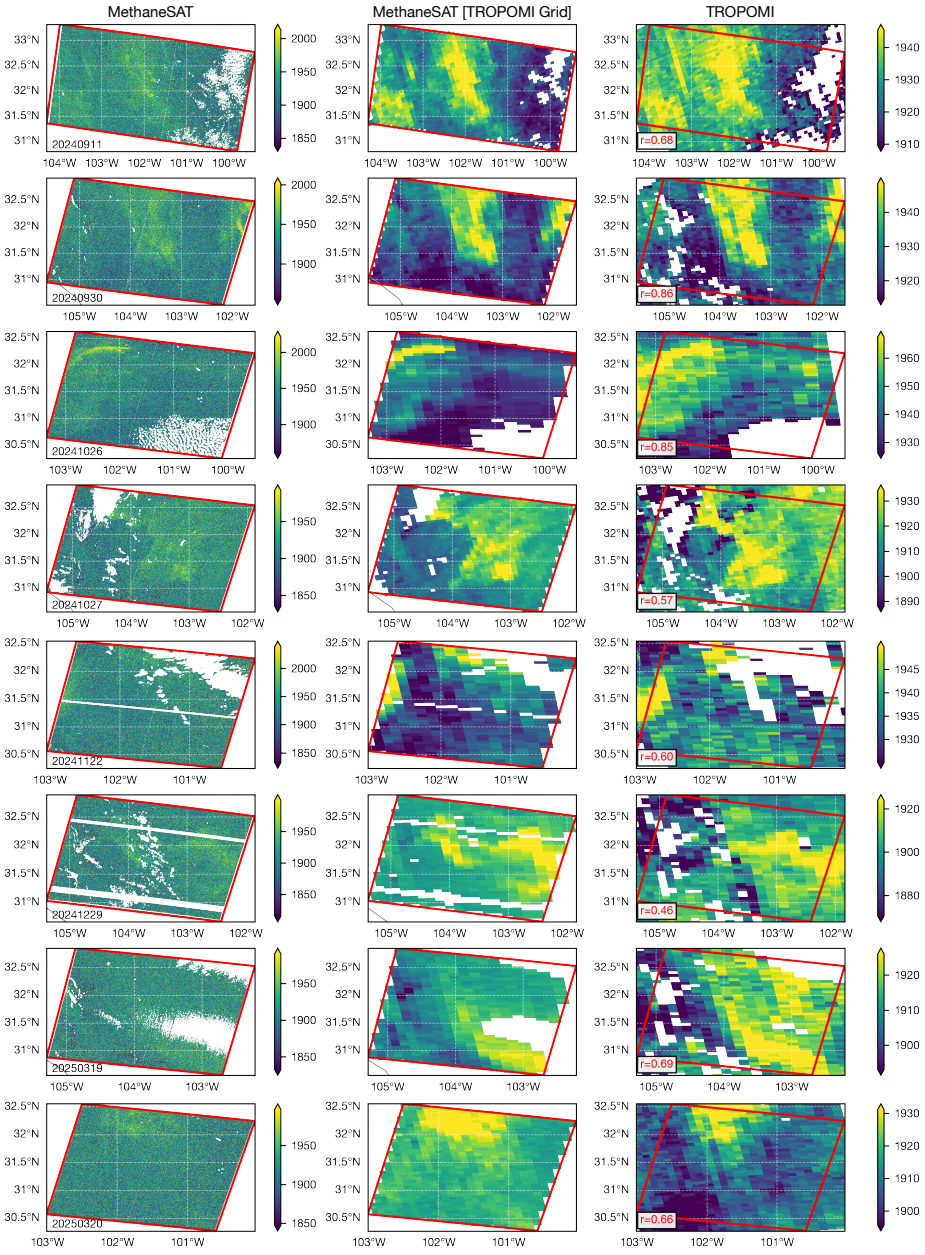

Figure 12. Comparison of X_{CH_4} enhancements over the Permian Basin observed by MethaneSAT and TROPOMI. Shown are MethaneSAT scenes acquired within one hour of the nearest TROPOMI overpass and with at least 80% cloud-free coverage. The left and right columns show MethaneSAT at native resolution, and averaged to the nearest TROPOMI pixel respectively. The right panel shows the TROPOMI X_{CH_4}, with the Pearson correlation with the aggregated MethaneSAT pixels indicated.

https://doi.org/10.5194/egusphere-2026-3365
Preprint. Discussion started: 3 July 2026

correlation coefficients ranging from 0.46 to 0.86. The weakest correlations occur in scenes with sub-TROPOMI-scale cloud contamination, where TROPOMI X_{CH_4} appear unphysically low near the edges of undetected clouds, most notably in the 2024-12-29 collection. This demonstrates the importance of MethaneSAT's higher spatial resolution for cloud clearing, as such anomalies are not present when aggregating to the TROPOMI resolution. MethaneSAT's higher spatial resolution also enables better separation of real features that could be interpreted as retrieval artifacts. For instance in the 2024-09-11 collection there appears to be a large stripe to the west of the main enhancement in TROPOMI. In the native resolution MethaneSAT image this is clearly identifiable as a plume aligned with the TROPOMI along-track direction.

4.3 Aerosol Dependence

Numerous studies have shown aerosols as an important source of systematic error in SWIR greenhouse gas retrievals, with mineral dust representing the the most dominant source globally (Houweling et al., 2005; Butz et al., 2010). The effect of dust is most pronounced over arid source regions, such as North Africa and the Middle East. Since these regions also contain many important oil and gas production zones, it is all the more important to evaluate the robustness of the proxy approach against dust.

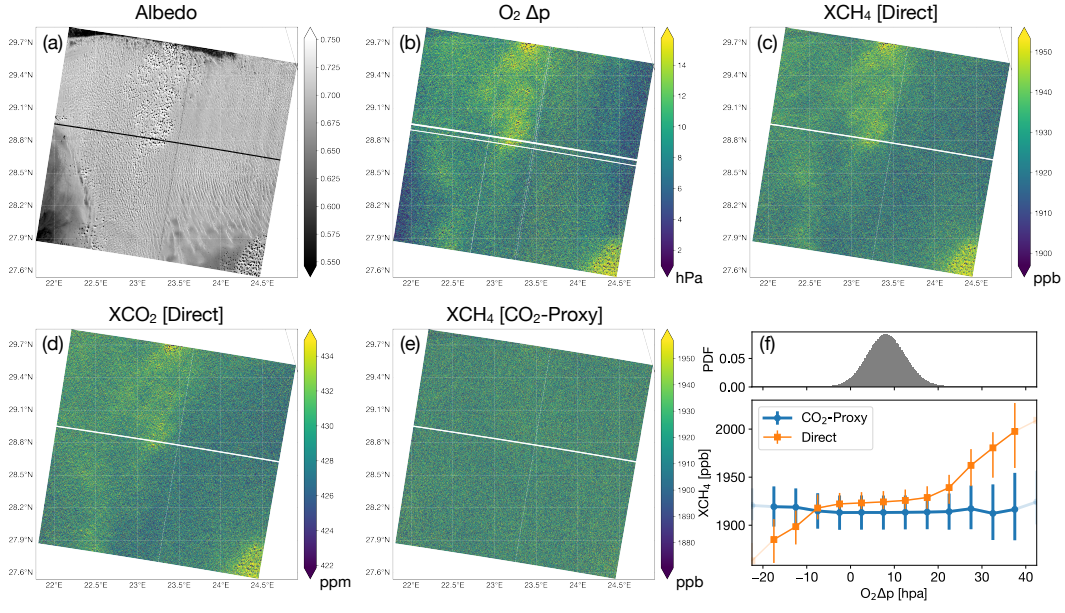

Figure 13. Example of aerosol- and cloud-induced light-path effects in a MethaneSAT desert calibration target. Shown is a representative MethaneSAT collection (Collection ID:04D90190, December 20, 2024) over the Libya4 Pseudo-Invariant Calibration Site (Chander et al., 2013), located far from major known CH_4 sources but frequently affected by dust. (a) shows the observation-derived albedo revealing low-level clouds. (b) The retrieved minus prior surface pressure difference from the oxygen band retrieval ($O_2\Delta p$). (c,d) Retrieved X_{CH_4} and X_{CO_2} normalized by the a priori dry-air column. (e) X_{CH_4} from the CO_2-proxy method. (f) compares retrieved X_{CH_4} with ($O_2\Delta p$)

https://doi.org/10.5194/egusphere-2026-3365
Preprint. Discussion started: 3 July 2026

Here we focus on the Libya4 Pseudo-Invariant Calibration Site (Chander et al., 2013), a CEOS-recommended desert calibration site located far from any major known CH_4 source but subject to frequently impacted by high dust levels. Figure 13 shows an example target observation. In this scene there is also scattering from low-level clouds in the upper center and bottom right of the image, visible from observation-derived albedo (Figure 13(a)).

To assess the magnitude of scattering-induced X_{CH_4}errors, we compare retrieved $X_{CH_4}$to the retrieved surface pressure change ($O_2\Delta p$), derived from a non-scattering retrieval in the $O_2(a^1\Delta_g)$ band. Since Rayleigh scattering is negligible and the a priori surface pressure is well constrained, large changes in $O_2\Delta p$ indicate aerosol-induced light path changes. As shown in Figure 13(b), negative $O_2\Delta p$ over clouds corresponds to an effective light path shortening due to direct reflection. In contrast, positive $O_2\Delta p$ is observed in the clear regions immediately adjacent to clouds, indicating light path lengthening. This behaviour is consistent with neglected horizontal radiative transfer in the 1D non-scattering model used by the retrieval, whereby scattering from nearby clouds illuminates the clear-sky surface, adding additional photon paths longer than those from direct reflection from sun to surface.

The direct $X_{CH_4}$and X_{CO_2} computed by normalizing the retrieved vertical columns using a priori dry-air columns (Figure 13(c,d)) show similar spatial patterns to $O_2\Delta p$. This supports the interpretation that the changes in absolute columns are driven by scattering-induced light path changes. Notably, the sign of these changes are opposite of those observed by Massie et al. (2023) for OCO-2 X_{CO_2}. This likely reflects differences in retrieval methodology: Since the full-physics OCO-2 retrieval includes aerosols in the state vector, forward model errors due to 1D radiative transfer assumptions are compensated by reducing X_{CO_2} and increasing aerosol scattering. In contrast, our non-scattering retrieval maps all light path errors directly onto the retrieved gas columns.

Figure 13(e) shows the CO_2-Proxy X_{CH_4}. In contrast to the direct retrievals it exhibits almost no spatial variability, as expected for a calibration region. This behavior is exhibited more clearly in Figure 13(f), which bins the direct and CO_2-proxy X_{CH_4}as a function of $O_2\Delta p$. For the directly retrieved X_{CH_4}, large changes occur for $O_2\Delta p$ values below and above -10 hPa and 20 hPa respectively. These features are strongly suppressed by the proxy. Even within these limits, the direct retrieval bin-mean X_{CH_4}increases approximately linearly by $\sim$25 ppb across the -10 to 20 hPa range, further demonstrating the proxy's effectiveness in correcting for light path errors.

In the example above, we included all data retrieved within the scene to better illustrate the dust-induced light path effects on X_{CH_4}. For retrieval validation, however, the more relevant question is whether the CO_2-proxy approach remains effective after applying fit-quality and cloud filters. Figure 14 shows X_{CH_4}binned by $O_2\Delta p$ for the five Libyan targets currently processed, using these flags. The X_{CH_4}value for the $O_2\Delta p = 0$ bin has been subtracted to facilitate comparison across granules.

Four of the five granules show variations in X_{CH_4} predominantly within ± 1 ppb across the observed $O_2\Delta p$ range, sufficient to meet the missions systematic error requirement. The remaining granule (11-September-2024) shows larger variation of approximately 4 ppb, with 60% of observations exceeding the ± 1 ppb threshold indicated in Figure 14. In this case, the variation in the 11-September-2024 scene may reflect genuine X_{CH_4}structure rather than a scattering-induced bias. Figure 15 compares MethaneSAT observations to the CAMS $X_{CH_4}$for this scene. The retrieved $O_2\Delta p$ (Figure 15(b) indicates a light

https://doi.org/10.5194/egusphere-2026-3365
Preprint. Discussion started: 3 July 2026

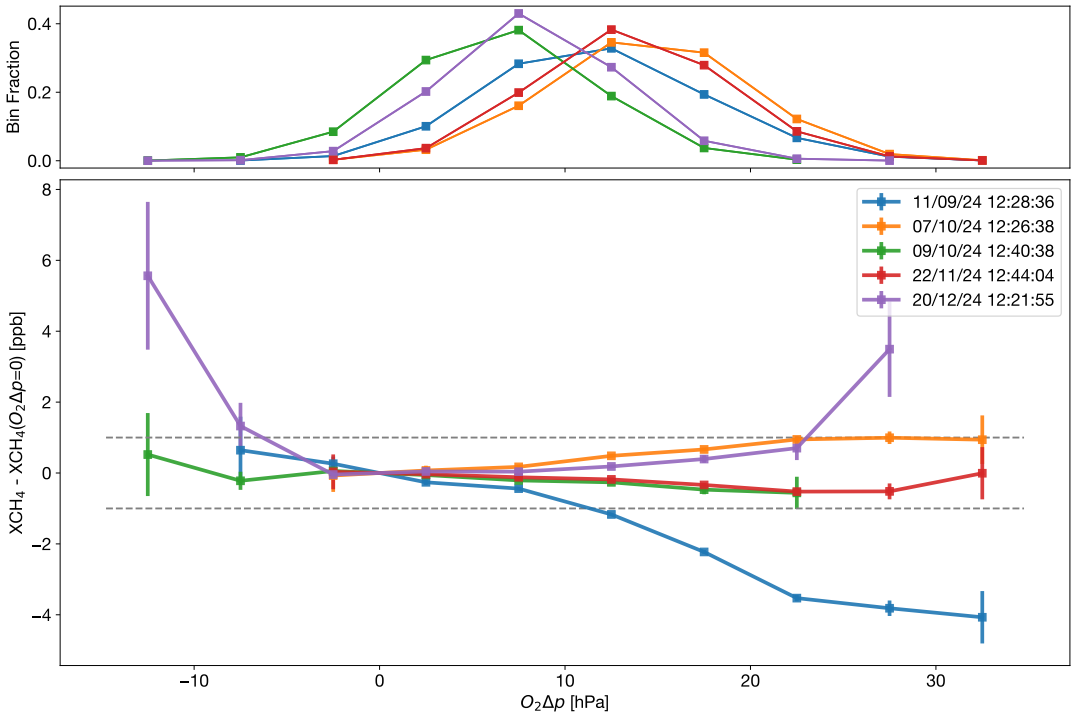

Figure 14. Assessment of residual dust-induced light-path effects on X_{CH_4} after cloud and quality screening. Shown is X_{CH_4} binned by retrieved O_2-band surface-pressure change ($O_2\Delta p$) for the five Libyan calibration targets currently processed, using standard fit-quality and cloud-screening flags, with the X_{CH_4} value in the $O_2\Delta p = 0$ bin subtracted to facilitate comparison across scenes.

path enhancement along the southern edge, a typical signature of aerosol scattering over bright surfaces (Butz et al., 2010). The MethaneSAT X_{CH_4} is anticorrelated with $O_2\Delta p$, producing the relationship shown in Figure 14.

CAMS, meanwhile, predicts a meridional X_{CH_4} gradient immediately north of the MethaneSAT granule 15(d)). When shifted 1.5° south, this gradient aligns with that observed by MethaneSAT (15(e)). This offset, while non-negligible, could plausibly reflect a positional error in the CAMS forecast. Taken together, these results indicate that the CO_2 proxy X_{CH_4} retrieval is largely robust to aerosol-induced light-path effects, with the 11-September-2024 case potentially reflecting real X_{CH_4} variability rather than an aerosol bias.

4.4 Sub-Scene CO_2 variability

In Section 4.2 we demonstrated that an accurate X_{CO_2} prior is essential for quantitative comparisons with TROPOMI X_{CH_4}. In the current retrieval, the GGG2020 X_{CO_2} prior is nearly uniform over the scale of a MethaneSAT scene. A uniform offset between this prior and the truth does not degrade the retrievals ability to retrieve relative X_{CH_4} enhancements within the scene. As indicated by Equation 27, the absolute X_{CH_4} retrieval error is directly proportional to the X_{CO_2} prior bias, resulting in a uniform scaling of the X_{CH_4} field that affects both the background and enhancement equally. Because fractional a priori biases

https://doi.org/10.5194/egusphere-2026-3365
Preprint. Discussion started: 3 July 2026

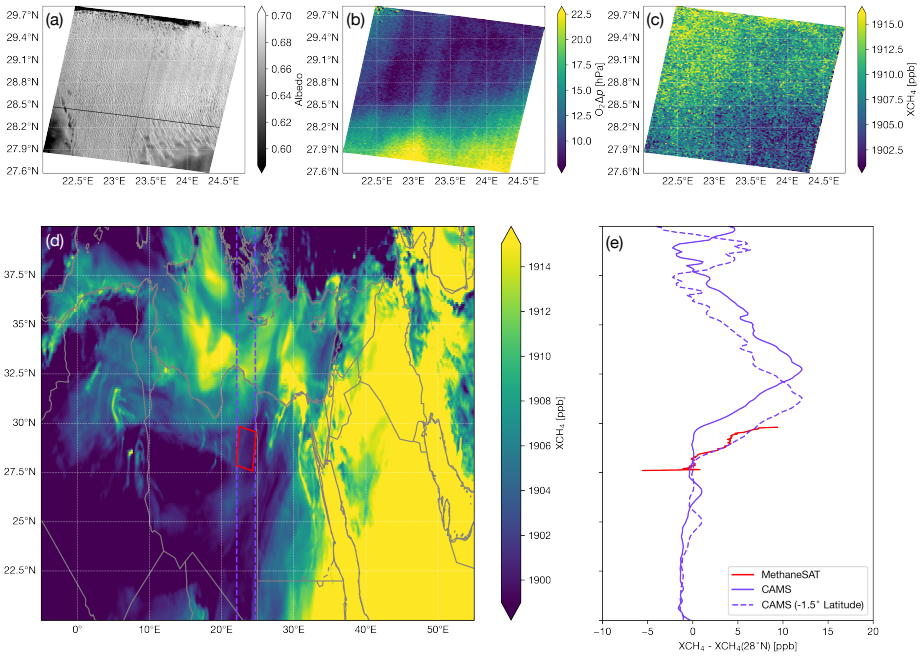

Figure 15. Assessment of dust-induced light-path effects versus genuine X_{CH_4} structure for the 11-September-2024 Libyan scene. (a) Scene albedo derived from 1621 nm MethaneSAT radiance (b) Retrieved minus prior surface pressure difference from O_2 band (c) MethaneSAT X_{CH_4}. (b) and (c) have been aggregated by a factor 4×20 along×across track to reduce noise. (d) X_{CH_4} from CAMS greenhouse Gas forecast at closest time to MethaneSAT observation (e) Longitudinal-average X_{CH_4} for CAMS (blue) and MethaneSAT (red). Dashed blue line is CAMS shifted 1.5°. The longitudinal band used for CAMS average is indicated by dashed blue line in (d).

in CO_2 are typically small ($< 1\%$), the bias in the retrieved enhancement is correspondingly small, and is much lower than other sources of uncertainty in the emissions inversion.

In contrast, subscene variabilty in X_{CO_2} that is not represented in the prior can be a far more significant error source. Spatially varying X_{CO_2} induces non-uniform scaling of the X_{CH_4} field, which can introduce artificial spatial structures that compete with, or even mask, emissions-induced enhancements within the scene. A variation of only a few ppm in X_{CO_2} across the scene is sufficient to generate ~ 9 ppb changes in X_{CH_4}, comparable in magnitude to typical O&G basin enhancements.

In the currently processed dataset, we were able to identify a few clear cases of subscene X_{CO_2} variability adversely impacting the retrieval. Figure 16 shows the most pronounced example, occurring over Ningxia province in northern China (Collection ID:06B506C0 , January 20, 2025). In this scene, CH_4 emissions from O&G infrastructure are concentrated in the Southeastern portion of the scene, whereas CO_2 emissions are predominantly over the urban core Yinchuan, located to the Southwest (Figure 16(a)).

The CO_2 emissions over Yinchuan are sufficiently strong to produce a X_{CO_2} enhancement exceeding 3 ppm, as evident in the direct X_{CO_2} (Figure 16(d)). In this case, we expect the X_{CO_2} retrieval to be reasonably accurate, as $O_2 \Delta p$ is near zero and

https://doi.org/10.5194/egusphere-2026-3365
Preprint. Discussion started: 3 July 2026

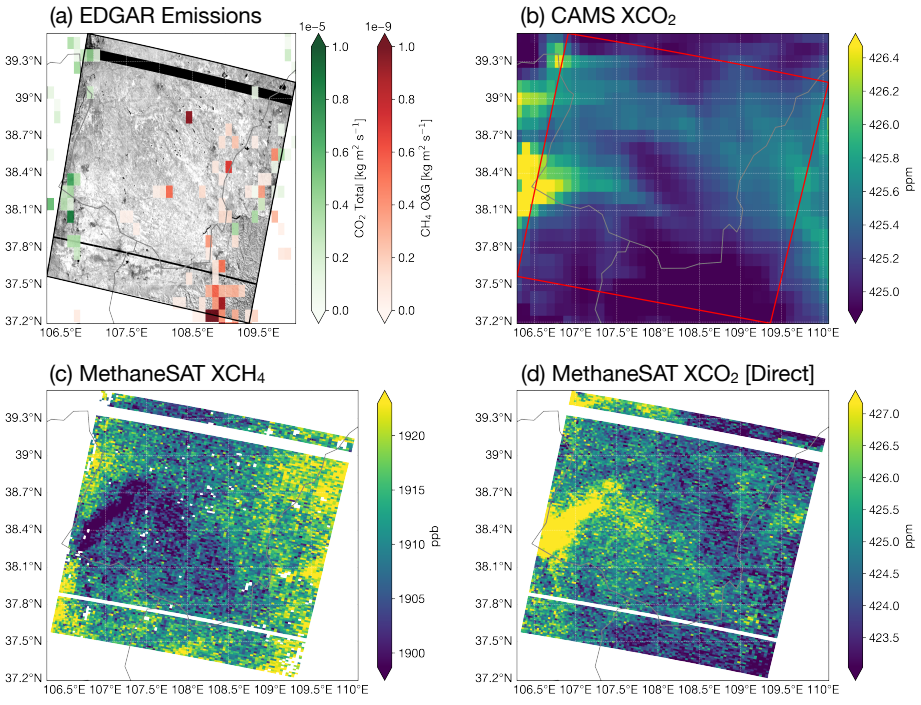

Figure 16. Example of strong subscene $X_{\mathrm{CO_2}}$ variability affecting the CO_2-proxy $X_{\mathrm{CH_4}}$ retrieval over Ningxia Province, northern China (Collection ID:06B506C0 , January 20, 2025). (a) Greyscale radiance overlayed with total CO_2 and O&G CH_4 2024 emissions from the EDGARv8.0 global emissions inventory (Crippa et al., 2024). (b) and (d) $X_{\mathrm{CO_2}}$ from CAMS global greenhouse gas forecast and MethaneSAT respectively. The MethaneSAT $X_{\mathrm{CO_2}}$ is calculated by normalizing the retrieved CO_2 column by the a priori dry-air column. (c) MethaneSAT CO_2-proxy $X_{\mathrm{CH_4}}$, showing a pronounced artificial reduction ("shadow") over Yinchuan induced by elevated CO_2.

spatially uniform across the scene. However, this enhanced CO_2 signal induces a pronounced "shadow" over Yinchuan in the CO_2-proxy $X_{\mathrm{CH_4}}$ field (Figure 16(c)). Conceptually, the proxy retrieval erroneously interprets the elevated CO_2 over the city as a light-path enhancement, resulting in an artificial decrease in the retrieved $X_{\mathrm{CH_4}}$.

Figure 16(b) shows the CAMS $X_{\mathrm{CO_2}}$ for the same scene. While CAMS reproduces the approximate location of the CO_2 enhancement, the magnitude of the plume is underestimated, and its orientation is more zonal than indicated by the observations. This example demonstrates that CAMS $X_{\mathrm{CO_2}}$ cannot be reliably used within the retrieval framework to correct for subscene $X_{\mathrm{CO_2}}$ variability. The magnitude and transport of local CO_2 sources are not represented with sufficient accuracy to accurately model subscene-scale $X_{\mathrm{CO_2}}$ variability, which will likely induce additional spatial biases in the CO_2-proxy $X_{\mathrm{CH_4}}$ retrieval.

The impact of subscene $X_{\mathrm{CO_2}}$ variability on the emissions inversion strongly depends on the relative spatial location of the CO_2 and CH_4 enhancements, making its overall effect on inferred emissions rates difficult to quantify. In the example above, the CO_2 and CH_4 emissions are spatially segregated. Within the current MethaneSAT inversion framework, the background $X_{\mathrm{CH_4}}$ used to infer the enhancement is defined using the 5^{th} percentile of $X_{\mathrm{CH_4}}$ within each scene. Suppression of $X_{\mathrm{CH_4}}$ over

https://doi.org/10.5194/egusphere-2026-3365
Preprint. Discussion started: 3 July 2026

the Yinchuan urban area therefore leads to an underestimation of the background, which in turn leads to spurious emissions placed at all regions outside the X_{CO_2} plume. At the opposite extreme, if CO_2 and CH_4 emissions were perfectly colocated, elevated CO_2 would act to dampen the observed CH_4 enhancement, leading to an underestimate of the inferred CH_4 emissions.

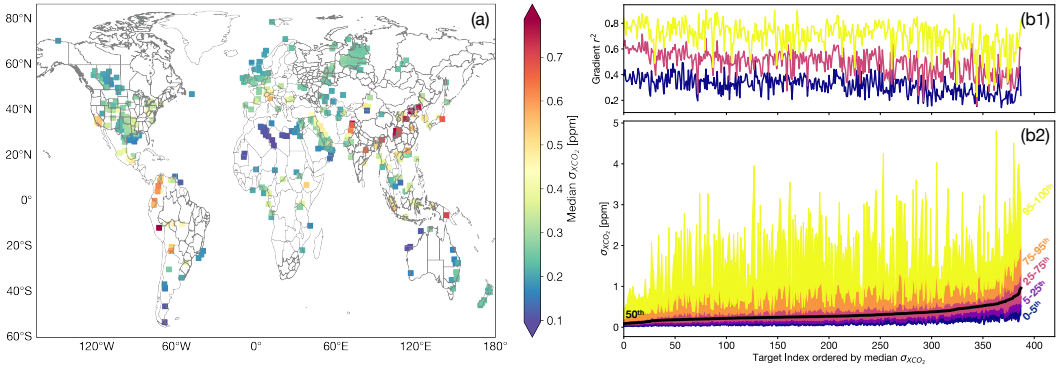

Figure 17. Subscene X_{CO_2} variability within MethaneSAT targets derived from CAMS forecasts (July 2024–June 2025). (a) Map of the median standard deviation of X_{CO_2} across all pixels within each MethaneSAT target, computed at each CAMS time step and summarized by the median over the full year. (b2) Distribution of $\sigma_{X_{CO_2}}$ across all targets ordered by median $\sigma_{X_{CO_2}}$, showing most targets exhibit low median variability but can occasionally experience high values. (b1) Mean fraction of variance explained by best-fit plane for targets grouped by $\sigma_{X_{CO_2}}$ percentile bins, showing increased contribution of large-scale gradients at higher variability levels.

To more broadly assess the impact of subscene CO_2 variability, we analyzed one year of CAMS global greenhouse gas forecast data (July 2024 - June 2025). For each CAMS timestep, we computed the standard deviation of X_{CO_2} across all pixels within each MethaneSAT target ($\sigma_{X_{CO_2}}$), using the boundaries defined in the MethaneSAT target deck shown in Figure 1. Figure 17(a) maps $\sigma_{X_{CO_2}}$ for each target, derived from the median across all CAMS time samples.

The highest median $\sigma_{X_{CO_2}}$ values occur over China, caused by the presence of large CO_2 sources within or nearby the targets. Elevated variability is also simulated for a subset of targets adjacent to mountain ranges, most notably over Peru near the Andes, California near the Sierra Nevada, and northern Pakistan near the Karakoram. In these regions, the high X_{CO_2} appears to be the result of topographic blocking and channeling of CO_2 emissions transported towards mountainous terrain, producing gradients in X_{CO_2} that correlate with surface elevation.

Figure 17(b2) shows the distribution of $\sigma_{X_{CO_2}}$ of each target, ordered by median $\sigma_{X_{CO_2}}$. Median $\sigma_{X_{CO_2}}$ variability levels are acceptable for most targets: 84% of targets have median $\sigma_{X_{CO_2}}$ below 0.45 ppm, limiting the standard deviation of the X_{CH_4} error induced from sub-scene X_{CO_2} variability to approximately 2 ppb. However, all targets can occasionally exhibit large $\sigma_{X_{CO_2}}$ values, with maxima ranging from 1-4 ppm. Because these elevated values also occur for targets with low median variability (i.e. targets with relatively small local X_{CO_2} emissions), they are likely driven by synoptic scale X_{CO_2} gradients.

To test this hypothesis, we computed the fraction of variance explained by the best-fit plane applied to the CAMS X_{CO_2} pixels within each target. The mean variance explained for the 0-5th, 25-75th, and 95-100th percentile bins of $\sigma_{X_{CO_2}}$ is shown in Figure 17(b1). As $\sigma_{X_{CO_2}}$ increases, the fitted plane explains an increasing fraction of the total variance, rising from an average

https://doi.org/10.5194/egusphere-2026-3365
Preprint. Discussion started: 3 July 2026

value of $r^2 = 0.32$ across all targets for the 0-5$^{\text{th}}$ bin to $r^2 = 0.72$ for the 95-100$^{\text{th}}$ bin. This trend indicates a transition from variability dominated by localized enhancements to variability dominated by large-scale background gradients.

In summary, subscene X_{CO_2} variability associated with either strong local CO_2 emissions and large-scale synoptic gradients likely represent the dominant sources of error in the CO_2-proxy X_{CH_4} retrieval. Large-scale screening using global simulations such as the CAMS greenhouse gas forecast may help identify scenes affected by synoptic gradients, which are generally more reliably represented by transport models. Additional improvements may also be achieved through refinements to how emissions inversions treat the background state. We showed that a significant fraction of the X_{CO_2} variability for scenes with high $\sigma_{X_{CO_2}}$ can be captured by fitting a plane to the X_{CO_2} field, corresponding to the inclusion of two additional background degrees of freedom. Emissions inversions could therefore consider incorporating such parameters as additional state vector elements to improve robustness against synoptic scale background errors.

For scenes influenced by complex topography, observed topographic gradients in X_{CH_4} may not only reflect the relative stratospheric vs. tropospheric contributions to the total column but also gradients in X_{CO_2} induced by topographic blocking of transported sources. In these cases parameterizing the background with an explicit altitude dependence may help mitigate retrieval biases.

For scenes dominated by strong local emissions, transport errors and uncertainties in a priori CO_2 emissions in global CO_2 simulations are unlikely to be accurate enough to accurately screen scenes for large subscene X_{CO_2} variability. In the current dataset, affected scenes are identified through manual inspection of the retrieved $O_2\Delta p$ and direct X_{CO_2} fields, with the corresponding L2 retrievals masked prior to emissions inversion. Automated screening will require approaches that utilize the observed data, potentially using X_{CO_2} estimated from the a priori dry-air columns like in Figure 16. In cases with low aerosol loadings, as identified through screening based on $O_2\Delta p$, the direct X_{CH_4} retrieval may be preferable to the CO_2-proxy approach. The use of the O_2 column as an alternal proxy may be viable due to its close proximity to the CH_4 band; however further work is needed to assess its sensitivity to inter-band differences in aerosol optical properties, and perhaps more importantly, surface albedo. As a final fallback, a full-physics retrieval may be required for the scenes with the highest local X_{CO_2} variability.

Although subscene X_{CO_2} variability likely represents the largest single source of error in the proxy retrieval, it occurs infrequently for most MethaneSAT targets; nevertheless, it remains an important effect to recognize and manage with the retrieval, and emissions inversion framework.

5 Conclusion and Implications for future missions

This study presents the first operational CH_4 retrievals from MethaneSAT using the CO_2-proxy method, and demonstrates that the instrument and retrieval framework meet the precision and accuracy requirements needed to quantify methane emissions at the scale of individual O&G production basins.

A central focus of this work was identifying and mitigating systematic retrieval errors that can approach the magnitude of typical O&G basin enhancements. Sensitivity differences between retrieved CO_2 and CH_4 vertical columns, which correlate

https://doi.org/10.5194/egusphere-2026-3365
Preprint. Discussion started: 3 July 2026

with albedo, were found to be a major potential bias source. We reduced these albedo-dependent errors to acceptable levels by tuning the a priori covariance matrix. Striping was identified as another major systematic error. We show that X_{CH_4} stripe biases strongly correlate with variations in the ISRF, and we develop a regression-based correction that removes most of this effect. A subsequent wavelet-Fourier filter eliminates most of the remaining striping, reducing stripe noise to levels suitable for emissions inversion.

Based on analyzing MethaneSAT retrievals over homogeneous validation scenes, we estimate X_{CH_4} single-pixel precision as a function of radiance. We estimate a X_{CH_4} precision of 30 ppb at ~110 m × 400 m pixel resolution for a typical bare-ground O&G scene (0.4 albedo, 30° SZA), which translates to a precision of 3 ppb at 2×2 km^2 resolution. The mission requirement of 3 ppb at 5×5 km^2 is met across all valid albedos and viewing geometries. Comparisons against TROPOMI show excellent overall accuracy: MethaneSAT agrees within 0.1 ppb averaged across all colocations, with a regression slope of 0.99 when using the CAMS greenhouse gas forecast as the X_{CO_2} prior. Both instruments show strong correspondence in the spatial pattern of Permian X_{CH_4} hotspots.

We further demonstrate that the CO_2-proxy method effectively mitigates aerosol- and cloud-induced light path errors after standard quality filtering, using observations over a frequently dusty calibration target in Libya. The most challenging remaining error source is sub-scene X_{CO_2} variability, where fluctuations of a few ppm can induce biases comparable to typical basin enhancements. Such conditions are likely infrequent for most MethaneSAT scenes but can occur in regions with strong local CO_2 emissions, complex topography, or pronounced synoptic gradients.

Overall, these results demonstrate that MethaneSAT has successfully achieved its primary objective of delivering X_{CH_4} observations with sufficient precision and systematic error control to enable robust basin-scale emissions estimates. They also highlight implications for current and future missions such as GOSAT-GW (Tanimoto et al., 2025) and CO2M (Sierk et al., 2021), both of which observe the 1.6 μm CH_4 band at moderately high resolution of 2 km × 2 km for CO2M and 1-3 km pixel size for GOSAT-GW in focus mode. These sensors can partially supplement the loss of MethaneSAT, though each has notable limitations. GOSAT-GW has a smaller 100×100 km^2 target mode, with an individual pixel precision of 30 ppb(Tanimoto et al., 2025). CO2M, with its wider 265 km swath, lacks target mode and has a 16 day repeat cycle that restricts target observation frequency; a constraint compounded further by cloud contamination. Nevertheless, the ability of these sensors to constrain regional fluxes, given their precision, spatial resolution, and area coverage, warrants further assessment and should be exploited to the extent possible.

Future work should prioritize treatment of basin-scale X_{CO_2} variability, which remains the primary limitation of the CO_2-proxy method. While N_2O has been proposed as an alternative proxy molecule for future missions to avoid this bias source, the factor of 8-10 reduction in precision relative to CO_2 (Frankenberg et al., 2025) would preclude the kind of single-target basin-scale inversions that MethaneSAT was designed to enable. The CO_2-proxy therefore remains the most viable approach for achieving the precision needed to constrain regional emissions, and improved strategies for characterizing and correcting sub-scene X_{CO_2} variability are essential to fully realize this potential.

https://doi.org/10.5194/egusphere-2026-3365
Preprint. Discussion started: 3 July 2026

Code and data availability. MethaneSAT products (Level 3 and above) are accessible via the Google Earth Engine Data Catalog (https://developers.google.com/earth-engine/datasets/tags/methanesat). Level 1b and Level 2 data are available via Google Cloud Storage, with access granted upon completion of a request form at https://forms.gle/jqw4Mvr63dsV1fUF8. TROPOMI data are available from the NASA Goddard Earth Sciences Data and Information Services Center (GES DISC) at https://disc.gsfc.nasa.gov. CAMS greenhouse gas forecast data are available from the Copernicus Atmosphere Monitoring Service at https://doi.org/10.24381/93910310. The retrieval code used in this study may be made available upon reasonable request, subject to organizational approval.

Author contributions. CCM analyzed the data and wrote the manuscript. CCM, SR, JSW, XL, KVC, and EW contributed to the scientific development of the L2 retrieval, and CCM, SR, DW, CH, and NL to its software implementation. BL, KS, JSB, MN, DJM, SC, NL, SA, and CC developed the L1b data product. RG and SW provided project leadership. SR, KS, DJM, and RG reviewed the manuscript.

Competing interests. The authors declare that they have no competing interests.

Acknowledgements. Funding for MethaneSAT and MethaneAIR activities was provided in part by an anonymous source, Arnold Ventures, The Audacious Project, Ballmer Group, Bezos Earth Fund, The Children's Investment Fund Foundation, Heising-Simons Family Fund, King Philanthropies, Robertson Foundation, Skyline Foundation, and Valhalla Foundation. For a more complete list of funders, please visit https://www.methanesat.org.

https://doi.org/10.5194/egusphere-2026-3365
Preprint. Discussion started: 3 July 2026

References

Results of the Anomaly Investigation into the Loss of Communication with MethaneSAT | MethaneSAT, https://www.methanesat.org/project-updates/results-anomaly-investigation-loss-communication-methanesat, 2025.

Borsdorff, T., aan de Brugh, J., Hu, H., Hasekamp, O., Sussmann, R., Rettinger, M., Hase, F., Gross, J., Schneider, M., Garcia, O., Stremme, W., Grutter, M., Feist, D. G., Arnold, S. G., De Mazière, M., Kumar Sha, M., Pollard, D. F., Kiel, M., Roehl, C., Wennberg, P. O., Toon, G. C., and Landgraf, J.: Mapping carbon monoxide pollution from space down to city scales with daily global coverage, Atmospheric Measurement Techniques, 11, 5507–5518, https://doi.org/10.5194/amt-11-5507-2018, 2018.

Butz, A., Hasekamp, O. P., Frankenberg, C., Vidot, J., and Aben, I.: CH4 retrievals from space-based solar backscatter measurements: Performance evaluation against simulated aerosol and cirrus loaded scenes, Journal of Geophysical Research: Atmospheres, 115, https://doi.org/10.1029/2010JD014514, _eprint: https://agupubs.onlinelibrary.wiley.com/doi/pdf/10.1029/2010JD014514, 2010.

Chan Miller, C., Roche, S., Wilzewski, J. S., Liu, X., Chance, K., Souri, A. H., Conway, E., Luo, B., Samra, J., Hawthorne, J., Sun, K., Staebell, C., Chulakadabba, A., Sargent, M., Benmergui, J. S., Franklin, J. E., Daube, B. C., Li, Y., Laughner, J. L., Baier, B. C., Gautam, R., Omara, M., and Wofsy, S. C.: Methane retrieval from MethaneAIR using the CO_2 proxy approach: a demonstration for the upcoming MethaneSAT mission, Atmospheric Measurement Techniques, 17, 5429–5454, https://doi.org/10.5194/amt-17-5429-2024, 2024.

Chander, G., Hewison, T. J., Fox, N., Wu, X., Xiong, X., and Blackwell, W. J.: Overview of Intercalibration of Satellite Instruments, IEEE Transactions on Geoscience and Remote Sensing, 51, 1056–1080, https://doi.org/10.1109/TGRS.2012.2228654, 2013.

Copernicus Atmosphere Monitoring Service, .: CAMS global greenhouse gas forecasts, https://doi.org/10.24381/93910310, 2024.

Crippa, M., Guizzardi, D., Pagani, F., Schiavina, M., Melchiorri, M., Pisoni, E., Graziosi, F., Muntean, M., Maes, J., Dijkstra, L., Van Damme, M., Clarisse, L., and Coheur, P.: Insights into the spatial distribution of global, national, and subnational greenhouse gas emissions in the Emissions Database for Global Atmospheric Research (EDGAR v8.0), Earth System Science Data, 16, 2811–2830, https://doi.org/10.5194/essd-16-2811-2024, 2024.

Cusworth, D. H., Thorpe, A. K., Ayasse, A. K., Stepp, D., Heckler, J., Asner, G. P., Miller, C. E., Yadav, V., Chapman, J. W., Eastwood, M. L., Green, R. O., Hmiel, B., Lyon, D. R., and Duren, R. M.: Strong methane point sources contribute a disproportionate fraction of total emissions across multiple basins in the United States, Proceedings of the National Academy of Sciences, 119, e2202338 119, https://doi.org/10.1073/pnas.2202338119, 2022.

Duren, R., Cusworth, D., Ayasse, A., Howell, K., Diamond, A., Scarpelli, T., Kim, J., O'neill, K., Lai-Norling, J., Thorpe, A., Zandbergen, S. R., Shaw, L., Keremedjiev, M., Guido, J., Giuliano, P., Goldstein, M., Nallapu, R., Barentsen, G., Thompson, D. R., Roth, K., Jensen, D., Eastwood, M., Reuland, F., Adams, T., Brandt, A., Kort, E. A., Mason, J., and Green, R. O.: The Carbon Mapper emissions monitoring system, Atmospheric Measurement Techniques, 18, 6933–6958, https://doi.org/10.5194/amt-18-6933-2025, 2025.

Frankenberg, C., Aben, I., Bergamaschi, P., Dlugokencky, E. J., van Hees, R., Houweling, S., van der Meer, P., Snel, R., and Tol, P.: Global column-averaged methane mixing ratios from 2003 to 2009 as derived from SCIAMACHY: Trends and variability, Journal of Geophysical Research: Atmospheres, 116, https://doi.org/10.1029/2010JD014849, _eprint: https://agupubs.onlinelibrary.wiley.com/doi/pdf/10.1029/2010JD014849, 2011.

Frankenberg, C., Sanghavi, S., Saha, A., Wennberg, P. O., Jacob, D. J., and Michalak, A. M.: On the Use of {\mathbfN_\mathbf2\O as a Light-Path Proxy for Accurate Greenhouse Gas Measurements From Space, Geophysical Research Letters, 52, e2024GL114 131, https://doi.org/10.1029/2024GL114131, _eprint: https://agupubs.onlinelibrary.wiley.com/doi/pdf/10.1029/2024GL114131, 2025.

https://doi.org/10.5194/egusphere-2026-3365
Preprint. Discussion started: 3 July 2026

Hasekamp, O., Lorente, A., Hu, H., Butz, A., ann de Brugh, J., Borsdorff, T., Martinez Velarte, M. C., Mandal, S., and Landgraf, J.: Algorithm Theoretical Baseline Document for Sentinel-5 Precursor Methane Retrieval, 2025.

Houweling, S., Hartmann, W., Aben, I., Schrijver, H., Skidmore, J., Roelofs, G.-J., and Breon, F.-M.: Evidence of systematic errors in SCIAMACHY-observed CO_2 due to aerosols, Atmospheric Chemistry and Physics, 5, 3003–3013, https://doi.org/10.5194/acp-5-3003-2005, 2005.

Hu, H., Hasekamp, O., Butz, A., Galli, A., Landgraf, J., Aan de Brugh, J., Borsdorff, T., Scheepmaker, R., and Aben, I.: The operational methane retrieval algorithm for TROPOMI, Atmospheric Measurement Techniques, 9, 5423–5440, https://doi.org/10.5194/amt-9-5423-2016, 2016.

Hu, H., Landgraf, J., Detmers, R., Borsdorff, T., Aan de Brugh, J., Aben, I., Butz, A., and Hasekamp, O.: Toward Global Mapping of Methane With TROPOMI: First Results and Intersatellite Comparison to GOSAT, Geophysical Research Letters, 45, 3682–3689, https://doi.org/10.1002/2018GL077259, _eprint: https://agupubs.onlinelibrary.wiley.com/doi/pdf/10.1002/2018GL077259, 2018.

Jervis, D., McKeever, J., Durak, B. O. A., Sloan, J. J., Gains, D., Varon, D. J., Ramier, A., Strupler, M., and Tarrant, E.: The GHGSat-D imaging spectrometer, Atmospheric Measurement Techniques, 14, 2127–2140, https://doi.org/10.5194/amt-14-2127-2021, 2021.

Kuze, A., Suto, H., Nakajima, M., and Hamazaki, T.: Thermal and near infrared sensor for carbon observation Fourier-transform spectrometer on the Greenhouse Gases Observing Satellite for greenhouse gases monitoring, Applied Optics, 48, 6716–6733, https://doi.org/10.1364/AO.48.006716, 2009.

Laughner, J. L., Roche, S., Kiel, M., Toon, G. C., Wunch, D., Baier, B. C., Biraud, S., Chen, H., Kivi, R., Laemmel, T., McKain, K., Quéhé, P.-Y., Rousogenous, C., Stephens, B. B., Walker, K., and Wennberg, P. O.: A new algorithm to generate a priori trace gas profiles for the GGG2020 retrieval algorithm, Atmospheric Measurement Techniques, 16, 1121–1146, https://doi.org/10.5194/amt-16-1121-2023, 2023.

Lorente, A., Borsdorff, T., Butz, A., Hasekamp, O., aan de Brugh, J., Schneider, A., Wu, L., Hase, F., Kivi, R., Wunch, D., Pollard, D. F., Shiomi, K., Deutscher, N. M., Velazco, V. A., Roehl, C. M., Wennberg, P. O., Warneke, T., and Landgraf, J.: Methane retrieved from TROPOMI: improvement of the data product and validation of the first 2 years of measurements, Atmospheric Measurement Techniques, 14, 665–684, https://doi.org/10.5194/amt-14-665-2021, 2021.

Lorente, A., Borsdorff, T., Martinez-Velarte, M. C., and Landgraf, J.: Accounting for surface reflectance spectral features in TROPOMI methane retrievals, Atmospheric Measurement Techniques, 16, 1597–1608, https://doi.org/10.5194/amt-16-1597-2023, 2023.

Massie, S. T., Cronk, H., Merrelli, A., Schmidt, S., and Mauceri, S.: Insights into 3D cloud radiative transfer effects for the Orbiting Carbon Observatory, Atmospheric Measurement Techniques, 16, 2145–2166, https://doi.org/10.5194/amt-16-2145-2023, 2023.

Mendonca, J., Strong, K., Toon, G. C., Wunch, D., Sung, K., Deutscher, N. M., Griffith, D. W. T., and Franklin, J. E.: Improving atmospheric CO2 retrievals using line mixing and speed-dependence when fitting high-resolution ground-based solar spectra, Journal of Molecular Spectroscopy, 323, 15–27, https://doi.org/10.1016/j.jms.2016.01.007, 2016.

Mendonca, J., Strong, K., Sung, K., Devi, V. M., Toon, G. C., Wunch, D., and Franklin, J. E.: Using high-resolution laboratory and ground-based solar spectra to assess CH4 absorption coefficient calculations, Journal of Quantitative Spectroscopy and Radiative Transfer, 190, 48–59, https://doi.org/10.1016/j.jqsrt.2016.12.013, 2017.

Mendonca, J., Strong, K., Wunch, D., Toon, G. C., Long, D. A., Hodges, J. T., Sironneau, V. T., and Franklin, J. E.: Using a speed-dependent Voigt line shape to retrieve O_2 from Total Carbon Column Observing Network solar spectra to improve measurements of XCO_2, Atmospheric Measurement Techniques, 12, 35–50, https://doi.org/10.5194/amt-12-35-2019, 2019.

https://doi.org/10.5194/egusphere-2026-3365
Preprint. Discussion started: 3 July 2026

Miller, D. J., Sun, K., Franklin, J. E., Leisso, N., Roche, S., Luo, B., Chan Miller, C., Ayvazov, S., Crowell, S., LoFaso, N., Kampe, T., Spuhler, P., Farris, B., Walker, E., Melendez, T., Gautam, R., Liu, X., and Wofsy, S. C.: MethaneSAT instrument spectral response functions during pre-launch calibration and on-orbit performance, EGUsphere, pp. 1–30, https://doi.org/10.5194/egusphere-2026-2675, 2026.

Münch, B., Trtik, P., Marone, F., and Stampanoni, M.: Stripe and ring artifact removal with combined wavelet — Fourier filtering, Optics Express, 17, 8567–8591, https://doi.org/10.1364/OE.17.008567, 2009.

NOAA/NWS/NCEP: Upgrade of the Global Forecast System (GFS) to Version 16, Tech. Rep. Service Change Notice 21-20, National Oceanic and Atmospheric Administration, https://www.weather.gov/media/notification/pdf2/scn21-20gfs_v16.0_aac.pdf, 2021.

Omara, M., Zavala-Araiza, D., Lyon, D. R., Hmiel, B., Roberts, K. A., and Hamburg, S. P.: Methane emissions from US low production oil and natural gas well sites, Nature Communications, 13, 2085, https://doi.org/10.1038/s41467-022-29709-3, 2022.

Rienecker, M. M., Suarez, M. J., Todling, R., Bacmeister, J., Takacs, L., Liu, H.-C., Gu, W., Sienkiewicz, M., Koster, R. D., Gelaro, R., Stajner, I., and Nielsen, J. E.: The GEOS-5 Data Assimilation System-Documentation of Versions 5.0.1, 5.1.0, and 5.2.0, Tech. Rep. NASA/TM-2008-104606-VOL-27, https://ntrs.nasa.gov/citations/20120011955, nTRS Author Affiliations: Goddard Space Flight Center, Science Applications International Corporation, University of Maryland, Baltimore County, Science Systems and Applications, Inc., Science Applications International Corporation NTRS Document ID: 20120011955 NTRS Research Center: Goddard Space Flight Center (GSFC), 2008.

Rodgers, C. D.: Inverse Methods for Atmospheric Sounding, WORLD SCIENTIFIC, https://doi.org/10.1142/3171, _eprint: https://www.worldscientific.com/doi/pdf/10.1142/3171, 2000.

Rodgers, C. D. and Connor, B. J.: Intercomparison of remote sounding instruments, Journal of Geophysical Research: Atmospheres, 108, https://doi.org/10.1029/2002JD002299, _eprint: https://agupubs.onlinelibrary.wiley.com/doi/pdf/10.1029/2002JD002299, 2003.

Saunois, M., Martinez, A., Poulter, B., Zhang, Z., Raymond, P. A., Regnier, P., Canadell, J. G., Jackson, R. B., Patra, P. K., Bousquet, P., Ciais, P., Dlugokencky, E. J., Lan, X., Allen, G. H., Bastviken, D., Beerling, D. J., Belikov, D. A., Blake, D. R., Castaldi, S., Crippa, M., Deemer, B. R., Dennison, F., Etiope, G., Gedney, N., Höglund-Isaksson, L., Holgerson, M. A., Hopcroft, P. O., Hugelius, G., Ito, A., Jain, A. K., Janardanan, R., Johnson, M. S., Kleinen, T., Krummel, P. B., Lauerwald, R., Li, T., Liu, X., McDonald, K. C., Melton, J. R., Mühle, J., Müller, J., Murguia-Flores, F., Niwa, Y., Noce, S., Pan, S., Parker, R. J., Peng, C., Ramonet, M., Riley, W. J., Rocher-Ros, G., Rosentreter, J. A., Sasakawa, M., Segers, A., Smith, S. J., Stanley, E. H., Thanwerdas, J., Tian, H., Tsuruta, A., Tubiello, F. N., Weber, T. S., van der Werf, G. R., Worthy, D. E. J., Xi, Y., Yoshida, Y., Zhang, W., Zheng, B., Zhu, Q., Zhu, Q., and Zhuang, Q.: Global Methane Budget 2000–2020, Earth System Science Data, 17, 1873–1958, https://doi.org/10.5194/essd-17-1873-2025, 2025.

Schneising, O., Buchwitz, M., Hachmeister, J., Vanselow, S., Reuter, M., Buschmann, M., Bovensmann, H., and Burrows, J. P.: Advances in retrieving XCH_4 and XCO from Sentinel-5 Precursor: improvements in the scientific TROPOMI/WFMD algorithm, Atmospheric Measurement Techniques, 16, 669–694, https://doi.org/10.5194/amt-16-669-2023, 2023.

Shindell, D., Ravishankara, A. R., Kuylenstierna, J. C. I., Michalopoulou, E., Höglund-Isaksson, L., Zhang, Y., Seltzer, K., Ru, M., Castelino, R., Faluvegi, G., Naik, V., Horowitz, L., He, J., Lamarque, J.-F., Sudo, K., Collins, W. J., Malley, C., Harmsen, M., Stark, K., Junkin, J., Li, G., Glick, A., and Borgford-Parnell, N.: Global Methane Assessment: Benefits and Costs of Mitigating Methane Emissions, https://ntrs.nasa.gov/citations/20210015658, nTRS Author Affiliations: Duke University, Colorado State University, Stockholm Environment Institute, International Institute for Applied Systems Analysis, Columbia University, NOAA Geophysical Fluid Dynamics Laboratory, National Center for Atmospheric Research, Nagoya University, University of Reading, Netherlands Environmental Assessment Agency, United Nations Environment Programme NTRS Report/Patent Number: Job No: DTI/2352/PA NTRS Document ID: 20210015658 NTRS Research Center: Goddard Space Flight Center (GSFC), 2021.

https://doi.org/10.5194/egusphere-2026-3365
Preprint. Discussion started: 3 July 2026

Sierk, B., Fernandez, V., Bézy, J.-L., Meijer, Y., Durand, Y., Courrèges-Lacoste, G. B., Pachot, C., Löscher, A., Nett, H., Minoglou, K., Boucher, L., Windpassinger, R., Pasquet, A., Serre, D., and Hennepe, F. t.: The Copernicus CO2M mission for monitoring anthropogenic carbon dioxide emissions from space, in: International Conference on Space Optics — ICSO 2020, vol. 11852, pp. 1563–1580, SPIE, https://doi.org/10.1117/12.2599613, 2021.

Suto, H., Kataoka, F., Kikuchi, N., Knuteson, R. O., Butz, A., Haun, M., Buijs, H., Shiomi, K., Imai, H., and Kuze, A.: Thermal and near-infrared sensor for carbon observation Fourier transform spectrometer-2 (TANSO-FTS-2) on the Greenhouse gases Observing SATellite-2 (GOSAT-2) during its first year in orbit, Atmospheric Measurement Techniques, 14, 2013–2039, https://doi.org/10.5194/amt-14-2013-2021, 2021.

Tanimoto, H., Matsunaga, T., Someya, Y., Fujinawa, T., Ohyama, H., Morino, I., Yashiro, H., Sugita, T., Inomata, S., Müller, A., Saeki, T., Yoshida, Y., Niwa, Y., Saito, M., Noda, H., Yamashita, Y., Ikeda, K., Saigusa, N., Machida, T., Frey, M. M., Lim, H., Srivastava, P., Jin, Y., Shimizu, A., Nishizawa, T., Kanaya, Y., Sekiya, T., Patra, P., Takigawa, M., Bisht, J., Kasai, Y., and Sato, T. O.: The greenhouse gas observation mission with Global Observing SATellite for Greenhouse gases and Water cycle (GOSAT-GW): objectives, conceptual framework and scientific contributions, Progress in Earth and Planetary Science, 12, 8, https://doi.org/10.1186/s40645-025-00684-9, 2025.

Taylor, T. E., O'Dell, C. W., Frankenberg, C., Partain, P. T., Cronk, H. Q., Savtchenko, A., Nelson, R. R., Rosenthal, E. J., Chang, A. Y., Fisher, B., Osterman, G. B., Pollock, R. H., Crisp, D., Eldering, A., and Gunson, M. R.: Orbiting Carbon Observatory-2 (OCO-2) cloud screening algorithms: validation against collocated MODIS and CALIOP data, Atmospheric Measurement Techniques, 9, 973–989, https://doi.org/10.5194/amt-9-973-2016, 2016.

Toon, G. C.: Atmospheric Voigt Line List for the TCCON 2020 Data Release, https://data.caltech.edu/records/zrkbg-re307, 2022a.

Toon, G. C.: Atmospheric Voigt Line List for the TCCON 2020 Data Release, https://data.caltech.edu/records/zrkbg-re307, 2022b.

United Nations Environment Programme: Global Methane Status Report, United Nations Environment Programme, https://doi.org/10.59117/20.500.11822/48921, 2025.

Varon, D. J., Jacob, D. J., Hmiel, B., Gautam, R., Lyon, D. R., Omara, M., Sulprizio, M., Shen, L., Pendergrass, D., Nesser, H., Qu, Z., Barkley, Z. R., Miles, N. L., Richardson, S. J., Davis, K. J., Pandey, S., Lu, X., Lorente, A., Borsdorff, T., Maasakkers, J. D., and Aben, I.: Continuous weekly monitoring of methane emissions from the Permian Basin by inversion of TROPOMI satellite observations, Atmospheric Chemistry and Physics, 23, 7503–7520, https://doi.org/10.5194/acp-23-7503-2023, 2023.

Veefkind, J. P., Serrano-Calvo, R., de Gouw, J., Dix, B., Schneising, O., Buchwitz, M., Barré, J., van der A, R. J., Liu, M., and Levelt, P. F.: Widespread Frequent Methane Emissions From the Oil and Gas Industry in the Permian Basin, Journal of Geophysical Research: Atmospheres, 128, e2022JD037 479, https://doi.org/10.1029/2022JD037479, _eprint: https://agupubs.onlinelibrary.wiley.com/doi/pdf/10.1029/2022JD037479, 2023.

Williams, J. P., Omara, M., Himmelberger, A., Zavala-Araiza, D., MacKay, K., Benmergui, J., Sargent, M., Wofsy, S. C., Hamburg, S. P., and Gautam, R.: Small emission sources in aggregate disproportionately account for a large majority of total methane emissions from the US oil and gas sector, Atmospheric Chemistry and Physics, 25, 1513–1532, https://doi.org/10.5194/acp-25-1513-2025, 2025.

Williams, J. P., Benmergui, J., Knapp, M., Omara, M., Himmelberger, A., Kyzivat, E., Weatherby, K., Lyke, B., Warren, J., MacKay, K., Ayvazov, S., Russi, M., LoFaso, N., Melendez, T., Miller, C. C., Roche, S., Sargent, M., Franklin, J., Nasr, M., Zhang, Z., Miller, D. J., Luo, B., Guanter, L., Hamburg, S. P., Wofsy, S. C., and Gautam, R.: Methane intensity and emissions across major oil and gas basins and individual jurisdictions using MethaneSAT observations, Atmospheric Chemistry and Physics, 26, 5961–5981, https://doi.org/10.5194/acp-26-5961-2026, 2026.

https://doi.org/10.5194/egusphere-2026-3365
Preprint. Discussion started: 3 July 2026

830 Zhang, Y., Gautam, R., Pandey, S., Omara, M., Maasakkers, J. D., Sadavarte, P., Lyon, D., Nesser, H., Sulprizio, M. P., Varon, D. J., Zhang, R., Houweling, S., Zavala-Araiza, D., Alvarez, R. A., Lorente, A., Hamburg, S. P., Aben, I., and Jacob, D. J.: Quantifying methane emissions from the largest oil-producing basin in the United States from space, Science Advances, 6, eaaz5120, https://doi.org/10.1126/sciadv.aaz5120, 2020.